Mineralium Deposita (2021) 56:381–406
https://doi.org/10.1007/s00126-020-00976-8

ARTICLE

Origin of a multi-stage epithermal Ag-Zn-Pb-Sn deposit: the Miocene Cortaderas breccia body, Pirquitas mine, NW Argentina

E. T. Slater[1] · D. J. Kontak[1] · A. M. Mcdonald[1] · M. Fayek[2]

Received: 5 June 2019 / Accepted: 12 March 2020 / Published online: 1 April 2020
© Springer-Verlag GmbH Germany, part of Springer Nature 2020

Abstract

The Miocene aged polymetallic (Ag-Zn-Sn-Pb) Pirquitas deposit of NW Argentina, hosted in an uplifted horst of Ordovician metaturbiditic rocks, defines the southern extent of the Andean Tin Belt. The nearby and recently discovered Cortaderas breccia-hosted Ag-Zn deposit contrasts markedly with the main Pirquitas deposit. To address these differences, a comprehensive geological, mineralogical, and geochemical study was undertaken and here reported. Ore formation commenced with brecciation and clay alteration of host rocks followed by six polymetallic ore stages and a waning stage. The complex mineralization (Ag, Sb, As, Sn, Fe, Zn, Cu, Pb, and Bi) consists of pyrite, marcasite, sphalerite, arsenopyrite, galena, cassiterite, quartz, dickite, siderite, hydrous phosphate minerals, and various sulfosalts and sulfides; metal assays indicate a telescoped system. Sphalerite-rich domains are characterized by massive, colloform, dendritic, and cockade textures. Silver and Sn principally occur in various sulfosalts (tetrahedrite, pyrargyrite, miargyrite, pirquitasite-hocartite, and canfieldite). Fluid inclusions reflect mixing of a ca. 5 wt% eq. NaCl fluid having a maximum Th value of 340 °C with heated meteoric water; in addition, fluid unmixing and flashing are documented to have accompanied ore formation. The $\delta^{34}S$ values for pyrite and sphalerite constrain $\delta^{34}S_{H2S}$ to ≈ 5‰ which suggests a magmatic reservoir. Collectively the data support a model, whereby the Cortaderas breccia reflects focusing of magmatic-sourced mineralizing fluids along an episodically dilating fault zone. Fluids ascended and depressurized following brecciation of the host rocks which initiated fast and slow boiling. The latter processes accounts for the intimate association of colloform- and dendritic-textured sphalerite. Subsequent sealing of the system allowed temperature gradients to rise which resulted in telescoping of the system and generation of this polymetallic ore zone.

Keywords Breccia · Silver · Zinc · Tin · Epithermal · Fluid inclusions · Andean Tin Belt

Introduction

The Pirquitas mine, located ~ 4250 m above sea level (masl) in the Puna plateau region, Jujuy province, NW Argentina, defines the southern limit of the richly mineralized Andean Tin Belt (ATB; Fig. 1a). It contains mineralogically diverse and texturally complex (e.g., colloform, dendritic) Ag-Zn-Sn-Pb mineralization as veins and breccias in an epizonal setting. The deposit has been mined since 1930 (Rosas and Avila 2013) with an historical production of ~ 777,600 kg of Ag, along with ~ 18,200 t of Sn prior to 2009 when modern open pit mining (Fig. 1d) commenced by SSR Mining (formerly Silver Standard Resources Inc.; Board et al. 2011). Since then, it has been a prolific producer of Ag with production exceeding 10 million ounces in 2016. Despite being an established mining camp known for high its Ag grades, little has been published in regard to its geology and mineralization (e.g., Malvicini 1978; Idoyaga 1995; Paar et al. 2001) with the recent work of Desanois et al. (2017, 2018) providing the most modern synthesis. The present paper expands on these earlier studies along with our own work (Slater 2016; Slater et al. 2019) by providing an overview of the regional and local geology and a summary of the historical deposit area, which provides the basis for assessing the nature of a new ore zone proximal the historical workings.

Editorial handling: B. Lehmann

Electronic supplementary material The online version of this article (https://doi.org/10.1007/s00126-020-00976-8) contains supplementary material, which is available to authorized users.

✉ E. T. Slater
esslater@gmail.com

[1] Harquail School of Earth Sciences, Laurentian University, 935 Ramsey Lake Road, Sudbury, Ontario P3E 2C6, Canada

[2] Department of Geological Sciences, University of Manitoba, Winnipeg, Manitoba R3T 2N2, Canada

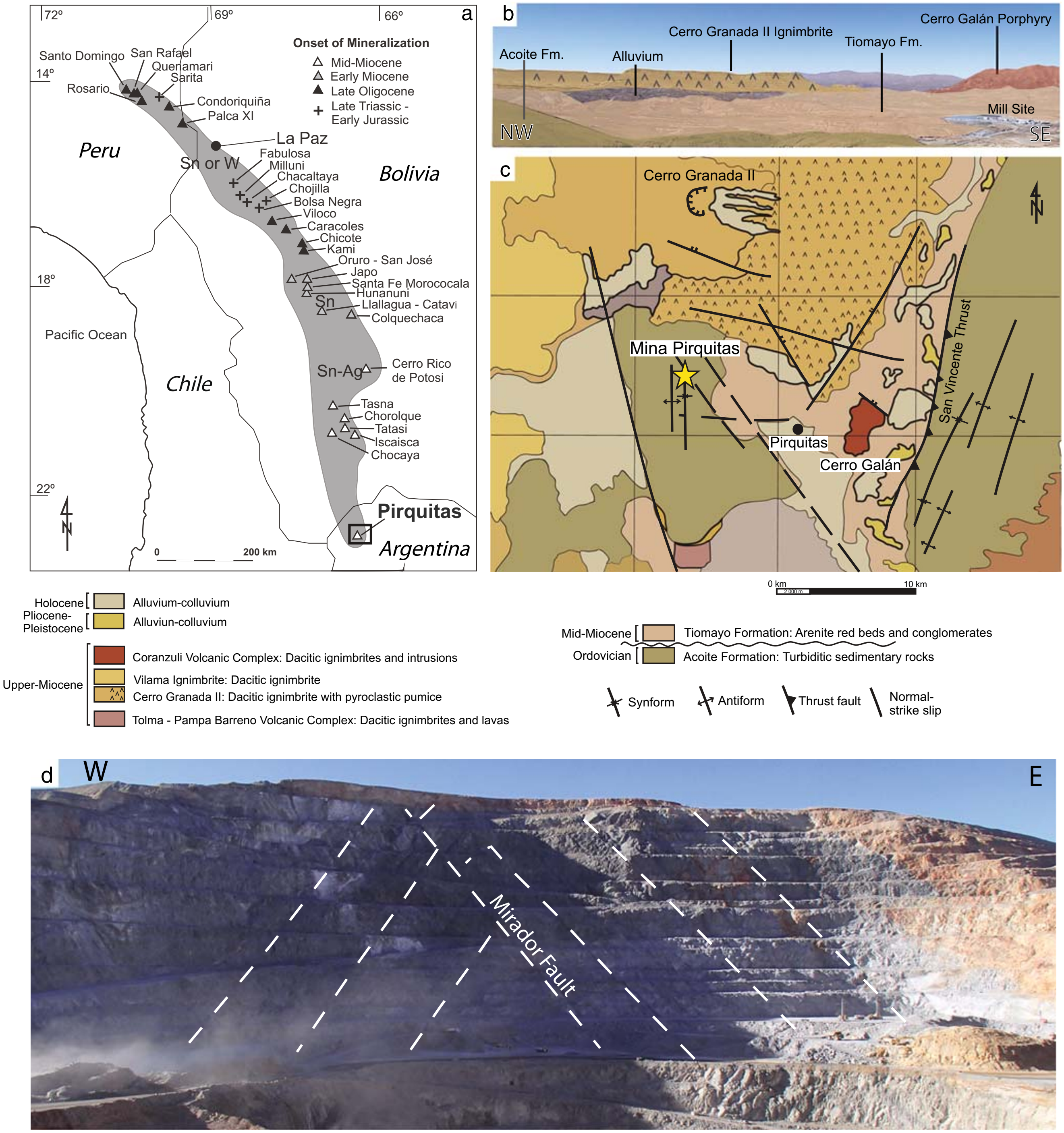

Fig. 1 **a** Geographic outline of the Central Andes showing the extent of the Andean Tin Belt (gray region) with noted deposits and their general ages (modified from Mlynarczyk and Williams-Jones 2005). The Pirquitas mine at the southern extent of the tin belt in northern Argentina is highlighted. **b** Annotated field photograph looking northeast and taken from top of an uplifted block of the Ordovician Acoite Formation with the major geological units in the area labeled. **c** Geological map of the Pirquitas mine area modified from (Coira et al. 2004). The yellow star indicates the location of the Pirquitas mine which is located in the uplifted basement rocks of the Acoite Formation. **d** Photograph looking approximately North in the Pirquitas Open pit (2013). The dashed white lines represent the bedding planes and the fault plane for the Mirador fault

In 2010, SSR Mining discovered the Ag-Zn-rich Cortaderas Breccia (herein Cortaderas) in the Cortaderas Valley zone located ~ 500 m north of the current open pit operation. The new zone contains an inferred resource of 23 Moz of Ag at 152 g/t, 360 Mlbs of Zn at 5.4%, and 6 Mlbs of Sn at 0.1% (NI 43–101 technical report: Board et al. 2011). This paper provides the first comprehensive description of the Cortaderas body and expands on our mineralogical focused study of the same material (Slater et al. 2019). Herein are presented data pertaining to its geological setting and mineralogy, alteration, and fluid chemistry (i.e., fluid inclusions, $\delta^{34}S$). In addition, grab samples from Potosi Breccia North, a large breccia body in the main Pirquitas deposit area, are characterized given the potential relevance of this breccia body to the origin of the Coraderas mineralization. Collectively these data are used to present a genetic model for the formation of the Cortaderas deposit.

Background

The Andean Tin Belt and its mineralization

The central Andes is host to precious- and base-metal deposits aligned in trench-parallel metallogenic belts (Petersen 1970) that include the following: the Andean Iron Belt with Fe-Cu-Mo-Au mineralization in the Western Cordillera (Sillitoe 2003), the Andean Copper Belt with Cu-Zn-Ag-Au-Mo mineralization in the Altiplano (Sillitoe and Perello 2005), and the ATB with Sn-W-Bi-Sb-Ag-Au mineralization in the Eastern Cordillera and Puna plateau (Lehmann et al. 1990). The ATB that stretches for ~ 900 km from southern Peru to northern Argentina includes two metallogenic episodes: late Triassic to early Jurassic and a more richly mineralized late Oligocene to middle Miocene one which includes the Pirquitas deposit (Fig. 1a). Both of these are linked to magmatic flare-ups corresponding to discrete collisional events between the South American and Nazca plates (Mlynarczyk and Williams-Jones 2005). In general, the northern deposits are Sn and W rich (e.g., San Judas Todeo: Clark et al. 1990; San Rafael: Kontak and Clark 2002; Wagner et al. 2009; and Palca 11: Farrar et al. 1990), whereas the southern counterparts are Sn and Ag rich (e.g., Cerro Rico de Potosi: Turneaure 1960a, b; Cunningham et al. 1996). As in Sn belts globally, the Andean granites related to Sn and W mineralization are generally reduced and hosted in carbonaceous sedimentary host rocks providing the chemical conditions necessary to keep magmas sufficiently reduced which is critical for generating Sn-rich fluids (e.g., Heinrich 1990; Linnen et al. 1995). In this regard, we note that the Pirquitas deposit area is hosted in an uplifted, deformed block of such metasedimentary material.

Models for the formation of Sn deposits in the ATB include Sn sourcing from a Sn-rich basement reservoir (Schuiling 1967; Kittl 1972; Clark et al. 1976; Schneider and Lehmann 1977) or the preferential extraction of Sn from a shallowly subducting slab beneath a thickened crust (Sillitoe 1972; Kay and Mpodozis 2001). Regarding the former model, Lehmann et al. (1988) studied the Ordovician-Silurian sedimentary basement rocks and found no underlying Sn enrichment, thereby excluding Sn-inheritance from basement rocks. Furthermore, subsequent geochemical studies by Lehmann et al. (1990) revealed systematic Sn enrichment in Bolivian granites that paralleled increasing Rb/Sr ratios; hence suggesting the Sn enrichment was related to magmatic evolution (i.e., fractional crystallization) and that the progenitor granites were not derived from a Sn-rich source area.

A variety of processes affecting ore fluids have been proposed to account for the epithermal or high-level Sn and base-metal mineralization throughout the ATB, including boiling, fluid mixing, depressurization, and cooling (e.g., Kelly and Turneaure 1970; Heinrich 1990; Kontak and Clark 2002; Wagner et al. 2009). These latter processes are in accord with the chemical modeling of Heinrich (1990), whereby he showed that each provide sufficient efficiency to generate high-grade Sn mineralization. As for high-grade base and precious metals, studies of epithermal deposits in Mexico and Peru, among others, have shown boiling to be an important process relevant to ore formation (e.g., Moncada et al. 2012, 2017; Gamarra-Urrunaga et al. 2013). As demonstrated below, our data for the Cortaderas deposit strongly suggest high-grade mineralization is localized to a system, whereby the ore fluid experienced both fluid unmixing and dilution by ingress of meteoric water.

Regional geology

The Pirquitas mine is located in the physiographic region known as the Puna plateau which was uplifted passively and through crustal shortening to elevations averaging 3700 masl during convergence of the South American and Nazca plates (Kay and Mpodozis 2001). Two stages of late Cenozoic deformation are recognized in the region (Cladouhos et al. 1994; Marrett et al. 1994). The first (~ 13 to 9 Ma) involved reverse faulting with an average shortening direction of 120° ± 20°, which differs from the average convergence direction of 82 ± 4° during that time and is attributed to reactivation of Cretaceous normal and strike-slip faults (Cladouhos et al. 1994). The second (9 Ma to recent) records diverse strain orientations, but has an average shortening direction of ENE-WSW. The latter was accommodated by strike-slip and, to a lesser extent, normal faulting as the Puna destabilized during uplift. From ~ 2 Ma to present, drainage basins developed which incised deep valleys and roughed the Puna's topography (Cladouhos et al. 1994).

The stratigraphy of northwestern Argentina is dominated by Ordovician metasedimentary rocks of the Santa Victoria Group (e.g., Turner and Mendez 1979; Turner 1982; Coira 1979; Coira et al. 2004). The uppermost member of this group, the Acoite Formation, is the only member of the Santa Victoria Group exposed in the Puna, and it constitutes the host rocks at Pirquitas and Cortaderas (Fig. 1b, c).

Originally described by Harrington (1957), the formation was reinterpreted by Bahlburg (1990) to be lithified clastic to volcano-clastic deep-water turbidite sequences deposited in a back-arc basin slope. At Pirquitas, these rocks comprise intercalated layers of quartzites, metapelites, and carbonaceous shales, whereas elsewhere they are interbedded with sparse metavolcanic rocks, including dacitic tuffs and dacitic to basaltic volcanic flows (Coira et al. 2004). These rocks were tightly folded and subjected to lower greenschist facies metamorphism during the Late-Ordovician Ocloyic orogeny (Turner and Mendez 1979; Bahlburg 1990) (e.g., Fig. 1d).

Foreland basins which formed during the Pehuenche tectonic phase from ~ 20 to 17 Ma contain the fluvio-lacustrine sedimentary and intercalated volcanic rocks of the Tiomayo Formation. The age of this formation is generally constrained from ~ 16 to 10 Ma by K-Ar dating of intercalated volcanic material (Coira et al. 2004). This formation is < 22 m thick and comprises arenites, conglomerates, siltstones, tuffs, and ignimbrites, but has great lateral variation. In the mine area (Fig. 1b, c), the unit discordantly overlies the Acoite Formation and consists of a basal conglomerate which grades upward into weakly consolidated arenites and mudstones. The strata are weakly deformed into homoclines and are locally affected by normal faults. Importantly, the K-Ar age of a gray ignimbrite intercalated with the reddish sediments in the lower levels of the Tiomayo Formation at Pirquitas constrains it to 14.9 ± 0.5 Ma (Coira et al. 2004).

Several felsic volcanic units occur in the surrounding area (Fig. 1b, c). Eruption of the Cerro Granada II ignimbrite at 9.8 Ma marked the onset of caldera-type volcanism in the region (Caffe et al. 2008). This high-K peraluminous dacitic ignimbrite with an aerial extent of 630 km^2 and volume of ~ 100 km^3 is centered ~ 12 km north of Pirquitas (Caffe et al. 2008). In contrast, the Vilama Caldera located to the NW of Pirquitas was active at 8.4 Ma and is estimated to have released ~ 1800 to 1200 km^3 of ejecta (Soler et al. 2007). The Coranzuli Volcanic Complex centered SE of Pirquitas includes the Coranzuli Caldera that was active at ~ 6.6 Ma and the Cerro Galán intrusion (Caffe et al. 2002).

Mine area geology and mineralization

Mineralization at the Pirquitas mine is hosted in an exhumed block of the folded Ordovician Acoite Formation (Figs. 1c, d, and 2a). The contained veins and breccia bodies, which are steeply dipping and discordant to the folded strata, are locally focussed along bedding contacts, fold hinges, and cut fold closures (e.g., Crucero vein: Fig. 2a). Furthermore, there is an apparent association between the location of fold hinges and mineralized veins. Vein data from Idoyaga (1995) show a dominant WNW-ESE trend (inset Fig. 2a). Several N-S trending faults mapped in the open pit (e.g., Mirador and Cortaderas; Figs. 1d, 2a) are traced at least as far north as Cortaderas with the Mirador fault, which parallels the limb of an anticline, having exploited a graphite-rich horizon in the sedimentary sequence. The absolute age of mineralization remains to be determined, but a maximum constraint is provided by veins, such as the Negra vein, which crosscut the basal remnants of the overlying ca. 15 Ma Tiomayo Formation (see above).

The most significant mineralized zones (i.e., areas considered prospective for exploration and mine development) are the San Miguel, Oploca, Cortaderas, and Huanuni (Fig. 2a). The San Miguel zone in the core of the open pit contains narrow sheeted veins and several larger ones. The latter includes the Potosi vein, with a known strike length of ~ 500 m and maximum thickness of 3 m, as well as the narrower Chocaya, Crucero, and Blanca veins, all of which have strike lengths of 50 to 150 m and are narrower. South of the San Miguel zone are the two Oploca veins, which are narrower, but with very high Ag concentrations. Approximately 500 m north of the San Miguel zone lies Cortaderas, which contains a sulfide-rich breccia body (≤ 20 m width) that grades outward into a broad zone of crackle breccias and smaller apophyses. To the NW of Cortaderas is the Huanuni zone, which contains several parallel and steeply dipping breccia veins with sulfide-rich mineralization.

The Cortaderas mineralized structure strikes ESE with a steep SW dip and has a minimum strike length of 500 m (Fig. 2a). The vein fill consists of pyrite, marcasite, sphalerite, arsenopyrite, galena, cassiterite, quartz, clays, mixed and Fe-carbonates, and various sulfosalts of Ag, Sb, As, Sn, Fe, Zn, Cu, Pb, and Bi. The mineralization is of varied texture (see below) and is dissected by the N-S trending Cortaderas and Mirador faults.

Previous studies of the Cortaderas and Pirquitas mineralization

In our earlier work (Slater 2016; Slater et al. 2019), the diverse mineralogy and textures of the Cortaderas mineralization were addressed. Several important findings were noted: (1) a secondary origin for some of the textures among the sulfides and sulfosalts related to unmixing of precursor minerals and assemblages; (2) the chemistry of Ag-bearing tetrahedrite, the dominant host for Ag, in two of the ore stages (see below) constrained formation temperatures between 245 and 270 °C; and (3) LA-ICP-MS analyses of color-banded sphalerite (i.e., variable Fe) and concentrically zoned pyrite from two stages indicated fluctuating amounts of many minor and trace metals which were attributed to cyclical dilation and sealing of the primary ore structure and which involved fluid mixing.

South of Cortaderas lies veins of the Pirquitas deposit proper, which are described below given the likely genetic association between these areas. Malvicini (1978) divided these veins into two groups, one early (Potosi, Blanca, Colquechaca,

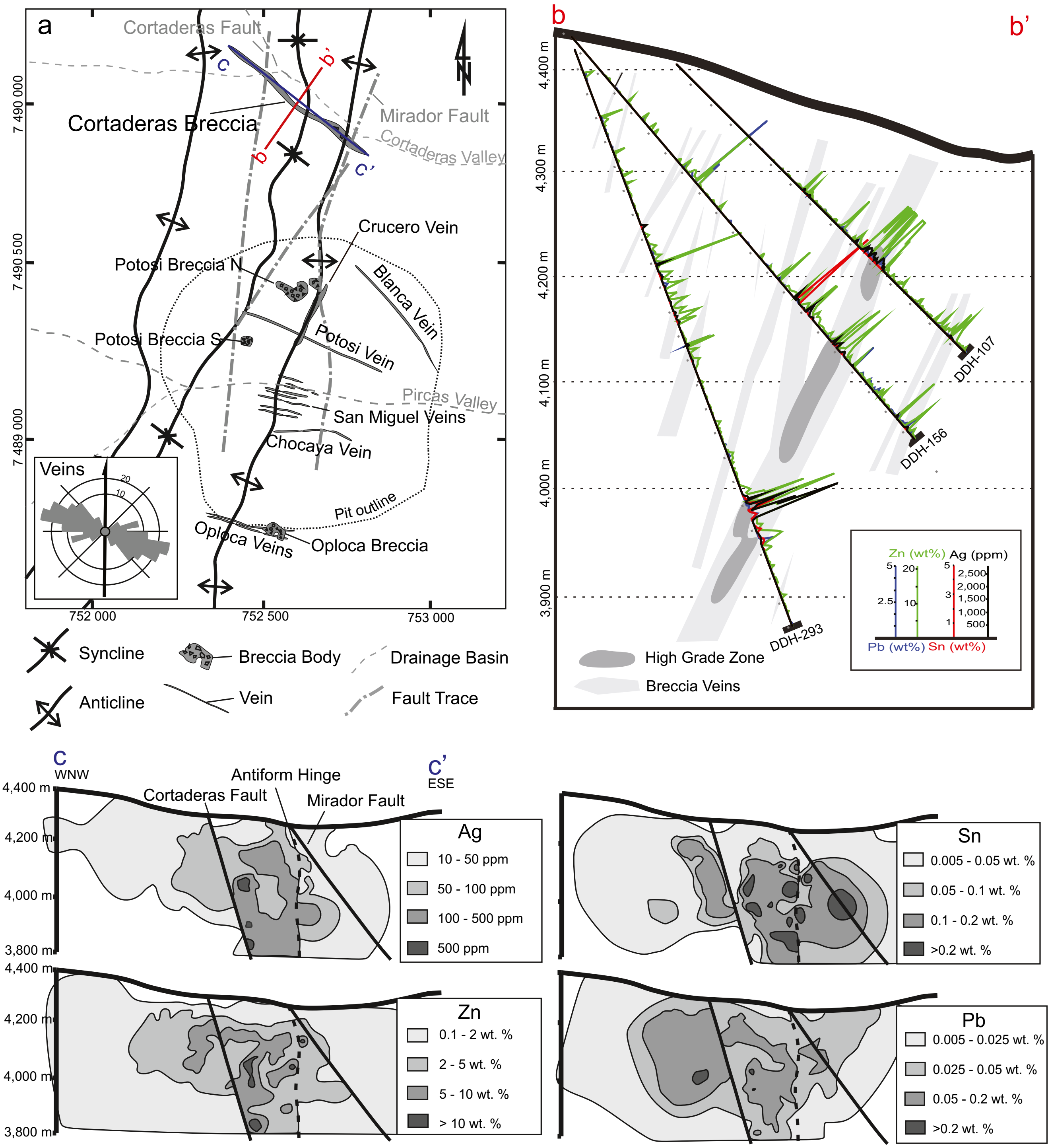

Fig. 2 **a** Plan map showing some of the major veins and breccia bodies in the Pirquitas mine area with a dotted black line denoting outline of the open pit as of 2013. Highlighted and discussed in the text are the sheeted San Miguel veins in the pit center, in addition to other large veins (Chocaya, Blanca, Potosi, the Oplocas, and Crucero), and the important breccia bodies (Potosi North, Potosi South and Oploca). Directly north of the pit is the Cortaderas Breccia, the subject of this study, which has characteristics of both the veins and of breccias. Inset is a rose diagram depicting vein orientations (modified from Idoyaga 1995). Also shown are the north striking anticlinal and synclinal structures in the basement rocks of the Acoite Formation. **b** Schematic cross-section (line b-b' in Fig. 2a) of the Cortaderas Breccia with the high-grade ore zone indicated by the dark gray polygon. Other inferred mineralized zones shown in light gray are interpreted between drill holes based on geochemistry and drill core logging. Metal concentrations are shown for Ag, Sn, Zn and Pb with equal scaling between holes. **c** Longitudinal composite sections (line c-c' in Fig. 2a) through the Cortaderas Breccia showing interpolated grade shells for Ag, Zn, Sn and Pb. These grade shells should be treated as qualitative

Oploca, Llallagua, Chicharron, and Colquiri) and the other late (San Pedro, Chocaya, and San Miguel). The early veins are characterized by early and late substages with the former consisting of quartz, pyrite, pyrrhotite, arsenopyrite, cassiterite, and chalcedony, whereas the latter are vertically zoned and consist of sphalerite-wurtzite, galena and stannite group minerals in the lower levels, sphalerite-wurtzite, boulangerite, semseyite, and fizelyite in the upper levels, and argentopyrite, teallite, frankeite, pyrargyrite, miargyrite, argentite, and polybasite in near-surface levels. The second vein group is telescoped and extends to greater depths than those of the first group. Their mineralogy consists of quartz, cassiterite, pyrite, arsenopyrite, chlorite, chalcopyrite, sphalerite-wurtzite, stannodite, canfieldite, kesterite, freibergite, schimerite, schapbachite, alaskaite, bournonite, pyrargyrite, miargyrite, polybasite, stephanite, and native silver. Locally vugs contain barite, antimonite, kaolinite, and alunite. Malvicini (1978) assigned three stages to the aforementioned assemblages: (1) pre-ore host rock alteration; (2) early sulfide mineralization (Stage I1) that progressed into later sulfosalt stage (Stage I2); and (3) a second period of sulfosalt mineralization (Stage II).

Recently, Desanois et al. (2017, 2018) presented fluid chemical data for the Pirquitas mineralization, which incorporated Malvicini's (1978) paragenesis, using fluid inclusions (FIs) hosted in quartz, sphalerite, Ag-Sn sulfides, and Ag-rich sulfosalts. Their results indicated the following: (1) stage I1 quartz-hosted FIs yielded homogenization temperatures (Th) of 233 to 370 °C and salinities of 0.9–4.3 wt% eq. NaCl; (2) stage I2 Ag-Sn-sulfides hosting FIs yielded Th of 213 to 274 °C and salinities up to 10.6 wt% eq. NaCl; and (3) stage II sphalerite and pyrargyrite FIs yielded Th of 190 to 252 °C and salinities of 0.9–4.3 wt% eq. NaCl. The FIs, as observed at room temperature, were two-phase aqueous (L-V) types with no evidence of fluid unmixing. Analysis of noble gases extracted from FIs suggested a significant magmatic component to the fluid. They interpreted the dataset as reflecting a decrease of temperature and salinity through the paragenesis as the hydrothermal system waned and mixed with meteoric water.

Methods

Sample collection and preparation

The deposit study involved the senior author working at the Pirquitas mine (~ 3 months) to conduct field work, review diamond drill core (15 holes) and historical drill core logs, and compile and assess archived geochemical data. Detailed re-logs of drill core through three cross sections of Cortaderas deposit provided the basis for sampling. Additional review of drill core which intersected the Huanuni and San Miguel zones was also done. Representative drill core material was collected from Cortaderas (112), Huanuni (24), and from below the San Miguel zone (4). In addition, grab samples of veins and breccia material from the open pit included a suite of five specimens from the Potosi Breccia North. Sections of drill core and select grab samples were slabbed and polished to enhance observation of mineral textures.

Whole-rock geochemistry and geochemical modeling

Whole-rock geochemical data and diamond drill core logs were provided by SSR Mining, including metal values determined by inductively coupled plasma atomic emission spectroscopy (ICP-AES; see Board et al. 2011). Data quality was assured by assessing standards and blanks, detection limits, and visual review of drill core. The data were modeled spatially using geochemical and geological modeling software where interpolation was done by Radial Distance Function geostatistical methods. Using these methods, grade shells for the metals Ag, Zn, Sn, and Pb were created for Cortaderas, which incorporated independent interpolations within structurally bound domains. The grade shells were then used to produce longitudinal sections through Cortaderas in order to compare metal distributions. The grade shells were not created as part of a robust mineral resource estimate and thus should only be treated as qualitative.

Ore petrography and SEM-EDS analysis

The mineralogy and textures were determined using a JEOL JSM-6400 scanning electron microscope (SEM) equipped with an Oxford Instruments™ INCA energy dispersive spectrometer (EDS) in the Mineral Analytical Centre (MAC) at Laurentian University, Sudbury. Analyses were performed with a beam current of ~ 1 nA, an accelerating voltage of 20 kV and varying live counting times between 5 and 30 s. The K-series X-ray lines were used for S, Fe, Cu, and Zn, L-series X-ray lines for As, Ag, Cd, In, and Sn, and M-series X-ray lines for Pb and Bi.

Electron microprobe (EMP) analysis

The compositions of sulfosalts were determined quantitatively using a SX-50 Cameca electron microprobe (EMP) in the MAC, Laurentian University, Sudbury. The operating conditions were 20 kV and 20 nA with 10 s on the peak and 5 s on the background. The beam diameter was 5 μm. The standards were chalcopyrite (Fe, Cu, S), sphalerite (Zn), PtAs (As), Ag metal (Ag), Sn metal (Sn), RhSb (Sb), and PbTe (Pb).

Powdered X-ray diffraction (XRD)

Pore-bound clays from six areas were concentrated into six samples and crushed in silica crucibles. The concentrates were analyzed by a Philips™ PW-1710 powder X-ray diffractometer (XRD) in the MAC, Laurentian University, Sudbury. The equipment operated at CoKα radiation, a scan rate of 5–75° 2 , a step size of 0.02° 2 , and a count time of 2 s/step. Spectra interpretation and mineral identification were performed using Pan Analytical™ HighScore Plus software.

Fluid inclusion study

Following reconnaissance studies of many samples to find FIs most suitable for microthermometric study, two double-polished, 100 μm thick chips were made from sphalerite-rich samples whose mineralogy and chemistry had previously been characterized by petrography and SEM-EDS. Freezing and heating measurements on 123 FI were performed at the Fluid Inclusion Laboratory, Laurentian University using a Linkam THMSG600 heating-cooling stage coupled with an Olympus™ BX51 microscope; we note that whereas some photomicrographs presented below were taken with a Q-Imaging Rolera-XR infrared (IR) camera, no thermometric measurements were made using IR light. Calibration was carried out using synthetic FI standards containing pure H_2O (melting at 0 °C and critical behavior at 374.1 °C) and CO_2 (triple point of −56.6 °C).

The methodology of FI assemblages (FIAs; see Goldstein and Reynolds 1994) was used to characterize and select FI for study. Due to the general scarcity of FIs (but note that locally samples are inundated), in rare cases, data for a single FIs are used and treated as a FIA since groups of FIs could not be measured. Single FIs are listed only where they show no petrographic evidence for post-entrapment modification (i.e., necked shapes). Isochores and salinities were calculated using the HOKIEFLINCS Microsoft Excel spreadsheet (Steele-MacInnis et al. 2012). In addition to FI studies in sphalerite, more extensive petrographic study of numerous samples, including those with quartz-hosted FI, was conducted.

Sulfur isotopes

Sulfur isotopic data were collected for mineral separates of sphalerite (*n* = 5) and pyrite (*n* = 3) in addition to in situ spot analyses (*n* = 16), using secondary ion mass spectrometry (SIMS), along a traverse through a single sample of colloform-textured sphalerite. The data were collected at the University of Manitoba Stable Isotopes for Innovative Research Laboratory, Winnipeg, Canada. For sulfide separates, material was analyzed using a CostechTM 4010 Elemental Analyzer coupled with a Thermo FinniganTM Delta V Plus isotope-ratio mass-spectrometer via an open-split interface. Samples were analyzed three times nonconsecutively as a test of reproducibility. Isotopic ratios are reported relative to international standards of the Vienna Cañon Diablo Troilite (CDT). International standards (IAEA-S1, IAEA-S2, and IAEA-S3) were analyzed at the beginning, middle, and end of each run along with two internal sulfide standards which were treated as unknowns for quality control measures. The precision in $\delta^{34}S$ is estimated at ± 0.2‰, and in these runs, the latter unknowns of GAL (galena, $\delta^{34}S_{VCDT} = +4.0 \pm 0.2‰$, $n = 15$) and Maine Light (Ag_2S, $\delta^{34}S_{VCDT} = -31.0 \pm 0.3‰$) yielded results of + 3.9‰ and − 31.2‰, respectively. For SIMS analysis, the sample was first polished and cleaned in a series of sonic baths and subsequently sputter-coated with a thin Au coating. Ion detection was done on an ETP 133H electron multiplier coupled with an ion-counting system. The instrument operated with a 20 μm sputtering diameter, a 300 V sample offset, a − 9 keV secondary accelerating voltage, a 247 μm slit, an 18 ns dead time, and a mass resolving power of 347. Sulfur isotopes were ionized using a 2 nA primary beam of Cs^+ accelerated at 10 kV. Respective standards were analyzed multiple times during the sessions and spot-to-spot analysis indicates precision at ± 0.5‰. The data are reported as $\delta^{34}S$ (CDT) in per mil (‰).

Results

Defining the Cortaderas ore body

Mineralization in the Cortaderas Valley is structurally controlled consisting of a series of subparallel ESE-striking structures or breccia veins that dip steeply SW (Fig. 2a, b). Herein it is the high-grade zone within the central breccia that is generally referred to as it is the widest and carries the most metal tenor. This central breccia is locally over 20 m wide, strikes for over 500 m and has a vertical extent of at least 400 m and is open at depth (Fig. 2b). The ore body is offset by the Cortaderas fault which has an apparent right-lateral displacement of ~ 10 to 20 m, whereas the Mirador fault shows no apparent displacement.

The mineralized zone consists of an outer halo of weakly mineralized crackle breccias (Fig. 3a, b) and breccia-like veins that grade into the central breccia body which contains sulfide mineralization with open-space filling textures (Fig. 3c). The central breccia vein contains varied textured sulfide mineralization that includes massive, colloform, dendritic, and cockade. Several syn- and post-mineral breccias are present with heterolithic clasts including fragments of mineralization supported in a rock flour matrix (Fig. 3d); these are described in more detail below.

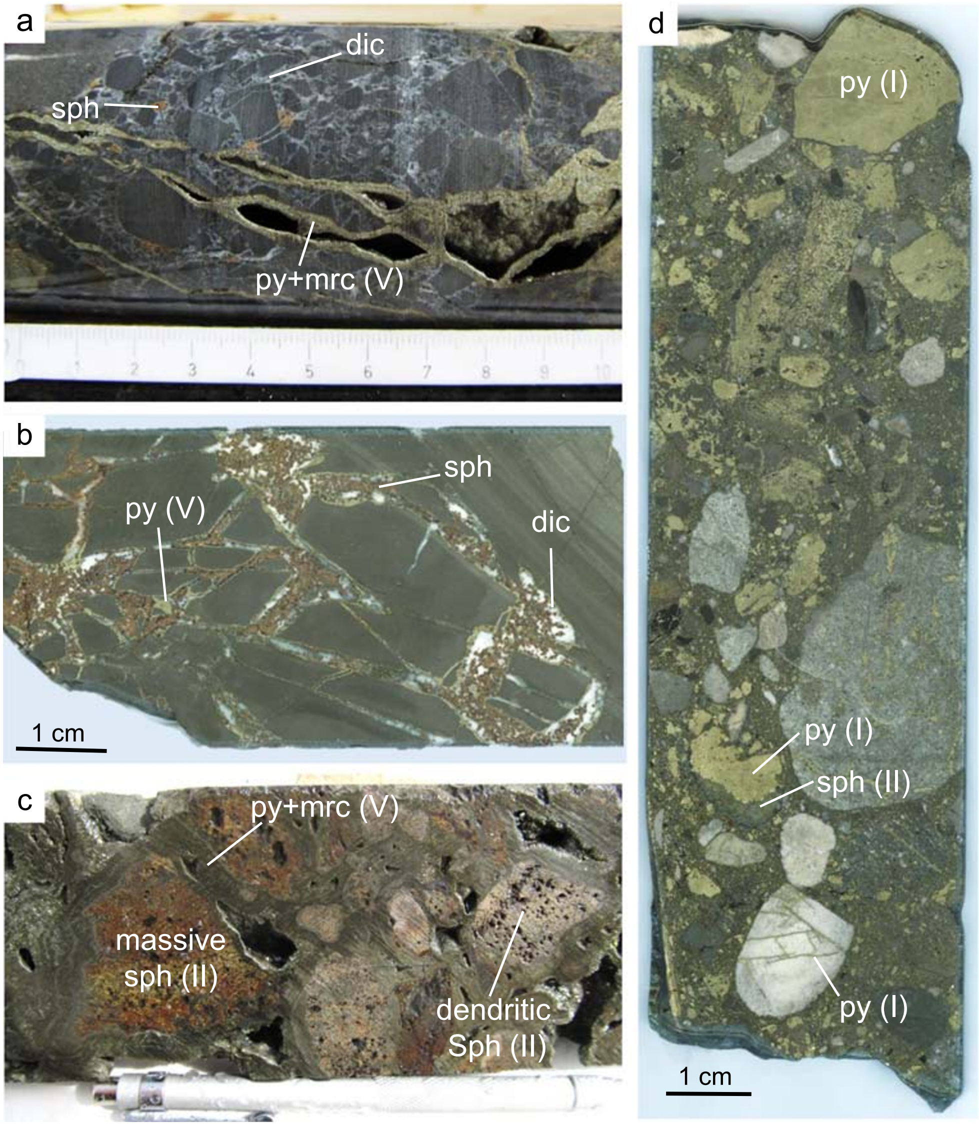

Fig. 3 Breccia samples seen in drill core. **a** Fault breccia with a weakly clay-altered (i.e., dickite (dic)) rock flour matrix. Colloform pyrite (py) and marcasite (mrc) coating fractures and openings that cut the breccia which is weakly mineralized with sphalerite (sph). **b** Crackle breccia with dickite, sphalerite and pyrite filling voids. Note thin alteration selvages locally. **c** Sulfide breccia with clasts of massive and dendritic sphalerite (sph) in matrix of colloform pyrite and marcasite. **d** Polylithic breccia with clasts of mineralization, and variably altered wall rock of sedimentary and probable igneous origin. The matrix is predominantly rock flour with some replacement by sphalerite and pyrite

Metal distributions

Modeling of lithogeochemical trends shows distinct metal zonations on the scale of the broader mine and exploration area. The San Miguel Zone in the centre of the Pirquitas deposit area (Fig. 2a) appears to be the core of the system, as it is enriched in Ag and Sn with Zn/Sn ratios increasing in the peripheral zones/veins. Cortaderas, being located far from the San Miguel zone (~ 500 m north), is Zn and Ag rich with lesser amounts of Sn. This same zonation is also apparent vertically with the deeper portions of the San Miguel zone being the most enriched in Sn and Ag.

In Cortaderas, there is good spatial correlation among concentrations of Ag, Sn, Zn, and Pb with the highest concentrations of the metals bound between the Cortaderas fault and the antiformal hinge plane of the folded Acoite Formation metasedimentary host rocks (Fig. 2c). Interestingly Pb and to some extent Zn are present in abundance to the west of the Cortaderas fault (Fig. 2c), which was also noted qualitatively in drill core based on the presence of sphalerite and galena. The Mirador fault appears to form the eastern boundary of the higher metal concentrations (Fig. 2c). Generally, high-metal concentrations are restricted to elevations below 4200 m and appear to increase with depth.

Breccia descriptions

A variety of breccia types are observed at Cortaderas—fault, crackle, phreatic, and pebble-dyke types (Fig. 3, ESM Table 1). The fault breccias are matrix to clast supported and contain rotated clasts of unmineralized angular wall rock in matrices of sericite-altered rock flour. Matrices contain minor amounts of disseminated sulfide mineralization (e.g., sphalerite) with clay. The crackle breccias are fracture arrays cemented by hydrothermal minerals, such as sphalerite, clay, siderite, quartz, pyrite, and marcasite; these minerals support mostly non-rotated angular clasts of wall rock (Fig. 3a). Powdered X-ray diffraction of this clay material shows it is dominantly dickite with one sample also containing kaolinite. In the central breccia vein, several episodes of mineralization and brecciation resulted in cockade textures with mineralized clasts supported by a sulfide matrix (Fig. 3c). Phreatic breccias are pipe- or vein-shaped bodies with rock-flour matrices that support rounded, heterolithic clasts of variably altered wall rock, as well as sulfide minerals (Fig. 3d, e). Pebble-dyke breccias are similar to the phreatic breccias but have a higher clast to matrix ratio.

The Potosi Breccia North is the largest breccia body in the Pirquitas area (Figs. 2a, 4). Although not part of Cortaderas, it plausibly has an important genetic link to its mineralization in addition to that at Pirquitas and was therefore studied. It is roughly cylindrical in shape, over 100 m wide, and has a known vertical extent of 250 m (Fig. 4a, b). This heterolithic body contains clasts of altered metasedimentary rocks, isolated quartz eyes of inferred igneous origin, and both clasts and matrix material originating from igneous protoliths (Fig. 4c–f). The matrix consists of rock flour (Fig. 4d), locally with fluidal-like texture, in addition to sulfides of sphalerite, galena, and pyrite (Fig. 4g). Sericite and clay are locally abundant often occurring as a pervasive alteration of clasts of igneous affinity (Fig. 4d). Furthermore, some clasts have porphyritic textures with relict feldspar phenocrysts and quartz eyes, whereas the presence of breccia clasts suggests multiple episodes of brecciation. As no clasts of mineralized material were observed, the Potosi Breccia North may predate observed mineralization at Pirquitas.

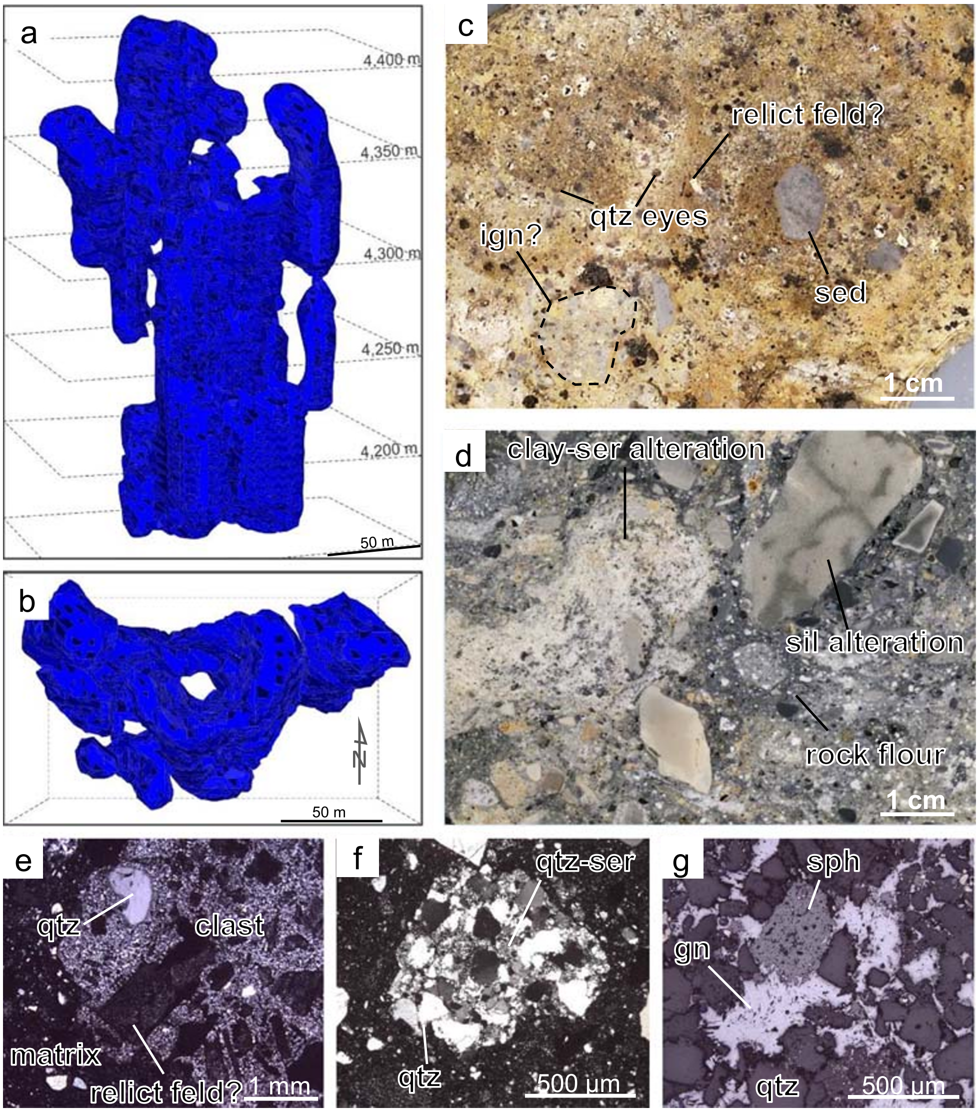

Fig. 4 Morphology and petrography of the Potosi Breccia North, the largest breccia body on the property. **a**, **b** Section (facing north) and plan view of the breccia pipe morphology (model provided by SSR Mining). **c** Cut grab sample of altered breccia with clasts of sedimentary rocks (sed) as well as some of probable igneous (ign?) origin. Quartz (qtz) eyes are abundant along with rarer feldspar and clots of clay and sulfide minerals. **d** Cut grab sample of more weakly altered breccia. Clasts of sedimentary rocks have silica (sil) alteration halos and selvages, where a sericite (ser) alteration is strongest in clasts of an igneous protolith. The matrix is dominantly gray rock flour. **e**, **f** Photomicrographs in cross-polarized transmitted light of clasts. **e** Rounded quartz eyes and tabular altered crystals, possibly relict feldspars (feld?) in a clast. **f** Seriate-textured quartz-rich clast with minor sericite. **g** Photomicrograph in reflected light of breccia matrix with sphalerite (sph) and galena (gn) cementing quartz (qtz) grains

Mineralization and alteration at Cortaderas

Mineralization at Cortaderas consists principally of sphalerite, pyrite, marcasite, arsenopyrite, cassiterite, galena, and various Ag-, Sn-, As-, Sb-, Pb-, Cu-, and Bi-bearing sulfosalts and sulfides, including those mentioned in the electronic supplementary material (ESM Table 2), which formed in several complex stages discussed below (Figs. 5, 6, and 7). In general, gangue minerals, which are subordinate to ore minerals, include quartz, dickite, and siderite as well as minor amounts of goyazite [$SrAl_3(PO_4)_2(OH)_5\bullet(H_2O)$] (ESM Fig. 1b); rarely unidentified REE-bearing hydrous phosphates are also present. Minor wall rock alteration occurs as selvages several millimeters to tens of centimeters wide that include clay, sericite, chlorite, and silica with minor sulfides (sphalerite, pyrite, marcasite). As noted above, XRD spectra revealed dickite to be the dominant clay mineral with rare kaolinite.

Pebble-dyke breccias locally contain mineralized clasts that differ from the typical ore zone material, as discussed in detail by Slater et al. (2019). For example, an unusual clast has massive pyrite coated by colloform cassiterite containing clots of Te-bearing canfieldite with fine-grained blebby inclusions of galena.

Paragenetic sequence

The complex mineral paragenesis at Cortaderas involves brecciation, mineral precipitation, metal remobilization, and related alteration. Based on observed mineral layering, crosscutting relationships, and mineral replacement textures, eight distinct and traceable stages are distinguished (Fig. 5a). Whereas the presented paragenesis may seem overly detailed, two points are noted: (1) examination of numerous samples demonstrates its robustness through the mineralized zone; and (2) it records significant changes in the evolution of the system as reflected by abrupt changes in mineralogy and elemental zoning in addition to textures. No single observed sample has all the stages, but several are often seen in single samples (Fig. 5b, c). The distinguishing features of each stage are described below.

Stage I

This stage is characterized by the mechanical preparation and alteration of the host rocks whereby hydraulic fracturing exploited a preexisting fault breccia to focus hydrothermal fluids that altered the wall rocks. This barren stage is

a		Pyritization (I)	Sph (II)	Ag (III)	Sph (IV)	Massive Sulfide (V)	Ag (VI)	Ag-Sn (VII)	Waning (VIII)
Gangue	Quartz	X	X	X		XX			X
	Sericite	X							X
	Clays					X			XXX
	Goyazite					X			X
	Siderite					X			X
Sulfides	Pyrite	XXX	X	XX		XXX	X	X	X
	Sphalerite		XXX	XX	XX	XX	X	X	
	Marcasite					XX			X
	Arsenopyrite		XX	XX			X	X	
	Galena		XX	XX				XX	
	Cassiterite			X		X		X	
Sulfosalts	Proustite-Pyrargyrite		X	X			X		
	Jordanite			X					
	Kesterite-Stannite			X		X	XXX	X	
	Smithite-Miargyrite			X			X		
	Ag-bearing Tetrahedrite			XX			X		
	Boulangerite			X					
	Frankeite							X	
	Canfieldite							XX	
	Pirquitasite-Hocartite							XX	

- - - - - - - - Brecciation **XXX** - Very Abundant **XX** - Abundant **X** - Present

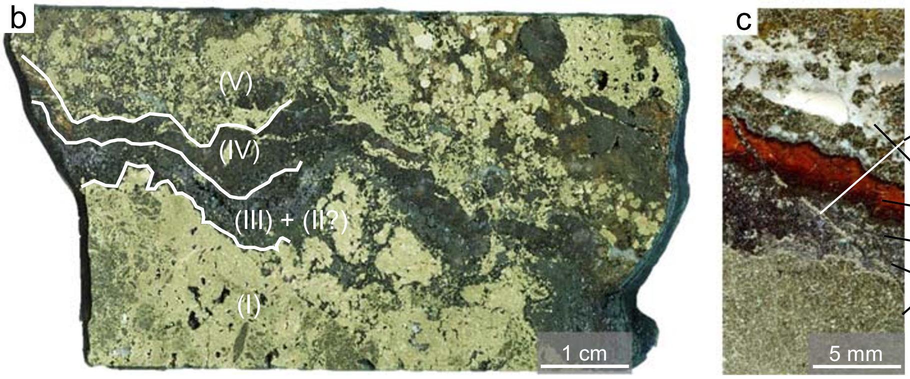

Fig. 5 **a** Paragenetic sequence showing the relative abundances of minerals deposited during each stage of mineralization in the Cortaderas Breccia. Note that all stages except IV and VII were preceded by a brecciation event, as indicated by the dashed lines. **b**, **c** Sample of drill core **b** and accompanying polished thick section **c** containing high-grade Ag mineralization. These samples are used to display the paragenetic stages, here stages I to VI, summarized in the previous figure

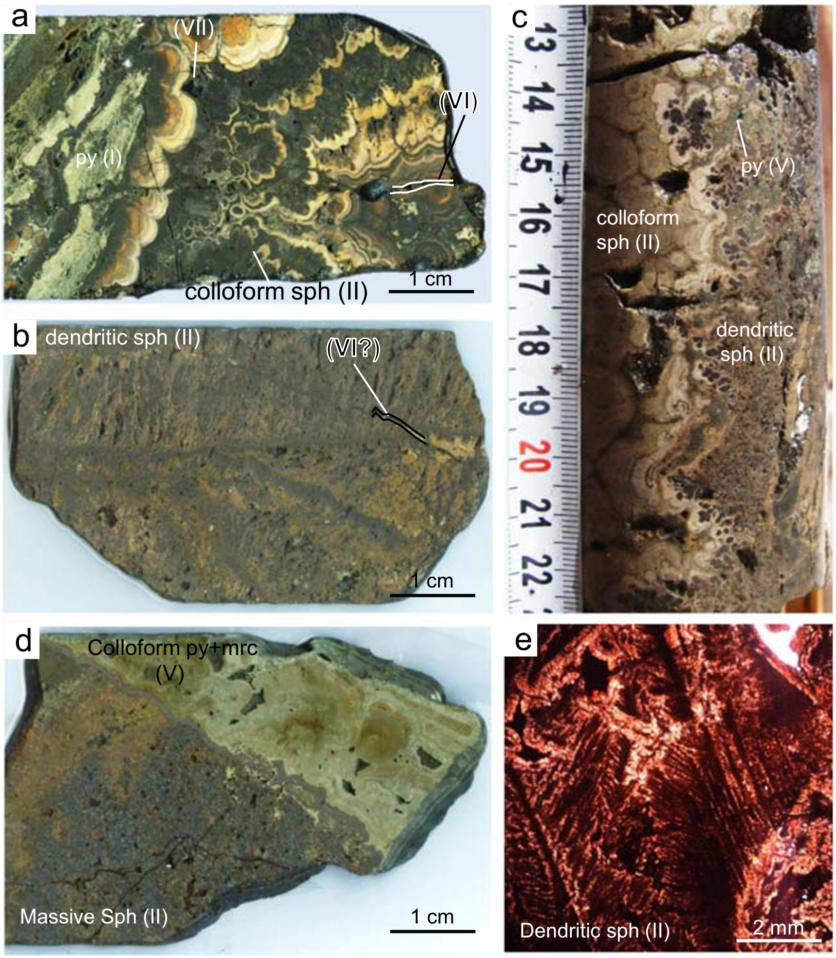

Fig. 6 Examples of colloform-, dendritic- and massive textures in drill core and polished thick sections of the mineralized Cortaderas Breccia. **a** Colloform-textured sphalerite (sph) of stage II showing several depositional cycles which nucleated on a clast of stage I pyrite (left side). **b** Dendritic sphalerite of stage II which also shows several depositional cycles. Cavity on right is lined with stage VI minerals. **c** Dark brown dendritic sphalerite that transitions into colloform textured, banded tan sphalerite. **d** Interlayered colloform pyrite (py) and marcasite (mrc) of stage V coating massive sphalerite of stage II. **e** Photomicrograph in plane light showing dendritic/feathery textured sphalerite of stage II

dominated by zones of fracture controlled (Fig. 3a, b) to massive pyrite due to replacement of wall rock clasts (Figs. 3d). Quartz and pyrite precipitated along fractures resulting in a vein stockwork; some of these are preserved in clasts (Fig. 3d). In addition, fracture-controlled and disseminated sericite and chlorite alteration is locally present. This stage likely equates to Malvicini's (1978) stage I1 at Pirquitas except that pyrrhotite is absent at Cortaderas but is observed at Pirquitas.

Stage II

This is the principal Zn stage and also marks the onset of Ag deposition. As such, sphalerite dominates (Fig. 6) with lesser galena, arsenopyrite and pyrite, and minor proustite (Fig. 7a–c). It formed following dilation and local brecciation which resulted in open-space-filling textures such as colloform, crustiform, dendritic, and massive (Figs. 3c and 6). Sphalerite textures vary with depth with coarsely banded crustification (Fig. 5c) in the upper parts, whereas finely laminated colloform and dendritic/feathery layers are at depth (Fig. 6). Colloform sphalerite exists as botryoidal masses composed of finely layered rhythmical color bands which transition from a dark brown to light tan in each depositional cycle (Fig. 6a–c. The dendritic type sphalerite occurs as branching aggregates of fine spherules occurring with colloform sphalerite (Fig. 6b–e). In general, dendritic sphalerite grades into colloform sphalerite (Fig. 6c). The sphalerite is intergrown with arsenopyrite and galena with the galena containing fine-grained blebby inclusions and larger globules of proustite (Fig. 7a, c) which are more abundant in galena at depth where sphalerite has a well-developed colloform texture.

Stage III

This is the main Ag stage and is characterized by having a crustiform texture (Fig. 5b, c) and a vertical zonation (Fig. 2c). It occurs as crusts on clasts and breccia walls indicating it post-dated brecciation. In the upper levels of the ore zone, this stage is characterized by narrow (< 10 cm wide) Pb-Sb-As-rich veins with galena, boulangerite, and jordanite where galena and jordanite are intergrown (Fig. 7d–f). When the two minerals are present, the galena is anhedral and highly porous with boulangerite filling these pores. At depth (i.e., below

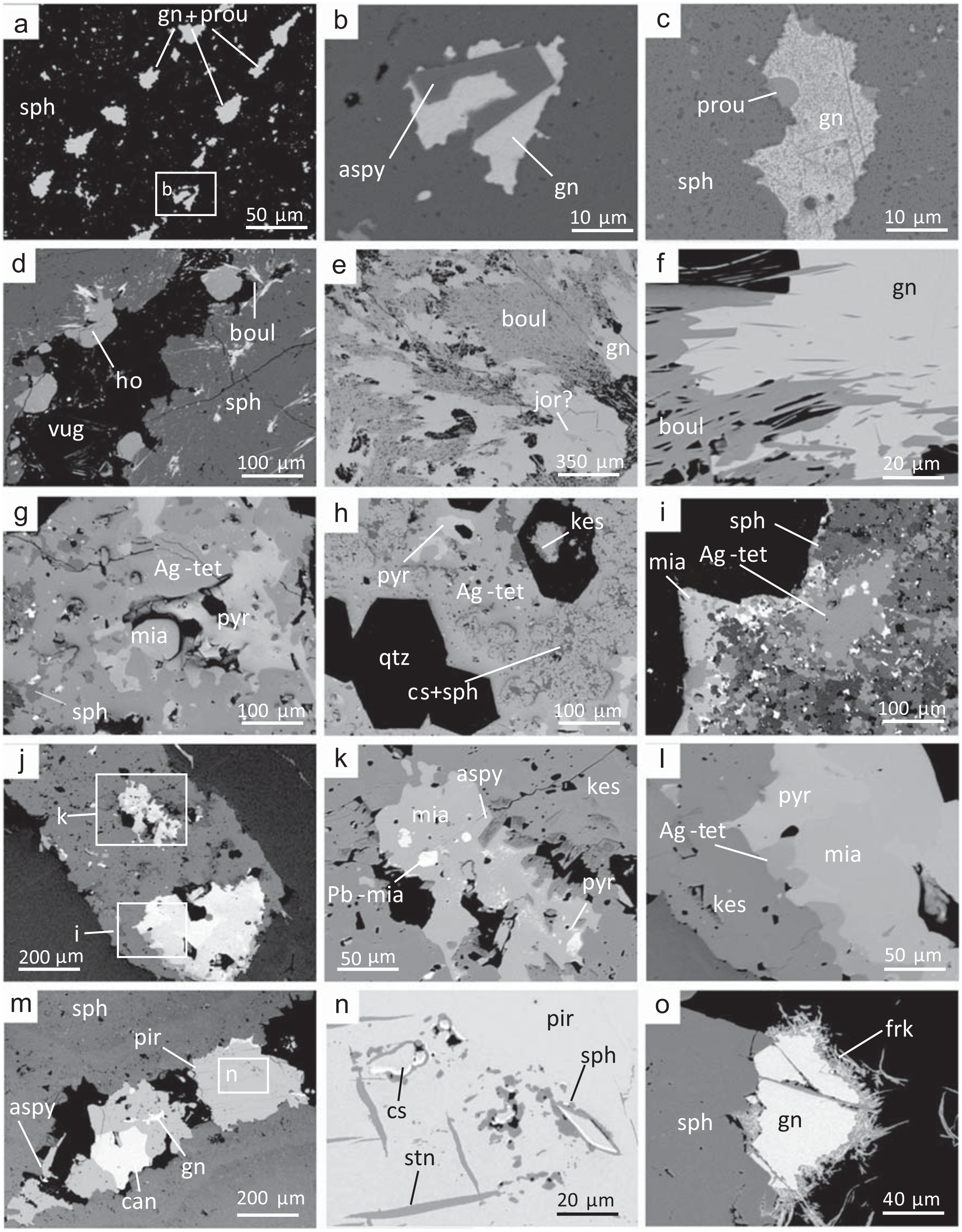

4150 masl), clasts of sulfide minerals and pyrite-altered wall rock are encrusted with dark sulfosalt-rich bands containing sphalerite, Ag-bearing tetrahedrite, pyrargyrite, miargyrite, an unidentified Ag-Sb-Pb-sulfosalt, pyrite, cassiterite, lesser amounts of kesterite, and minor amounts galena and unclassified Bi-Pb-bearing minerals (Fig. 7g–i). As noted above, tetrahedrite geothermometry yielded temperatures of 245 ± 15 °C for this stage (Slater et al. 2019).

Stage IV

This stage consists of a 0.2–1 cm thick band of weakly colloform to crustiform sphalerite (Fig. 5c) and appears to be concordant with stage III mineralization; therefore it may not have precipitated immediately following a brecciation event. The sphalerite is color banded with early-formed layers being light orange (< 1 wt% Fe) and the later layers dark brown (<

◀ **Fig. 7** Backscattered electron images of mineralization from several paragenetic stages (II, III, VI, and VII). **a**, **b**, **c** Polymetallic inclusions in colloform sphalerite (sph) of stage II. Galena (gn) locally contains blebby inclusions of proustite (prou) and in rare cases is intergrown with arsenopyrite (aspy). **d**, **e**, **f** Lead and Sb mineralization in stage III veins. Galena contains inclusions of possible jordanite (jor?) and is overgrown by boulangerite (boul). Sphalerite and hocartite of stage VII overgrow the boulangerite and exist in vugs. (**g**, **h**, **i**) Polymetallic mineralization of stage III occurs as 1–2 cm thick crust on clast of stage I pyrite. Main phases include Ag-bearing tetrahedrite (Ag-tet), pyrargyrite (pyr), miargyrite (mia), cassiterite (cs) and sphalerite. Minor amounts of Pb-Bi-Ag clots are present locally and appear as white specks in images "g" and "i". Euhedral quartz (qtz) often hosts inclusions of cassiterite, but predates most other minerals of this stage. **j**, **k**, **l** Polymetallic mineralization of stage VI, occurring as thin veinlets, mainly include kesterite (kes), pyrargyrite, miargyrite, and Ag-bearing tetrahedrite. Some Pb-Sb-bearing inclusions in miargyrite are present as white spots. **m**, **n**, **o** Polymetallic mineralization of stage VII, which occludes pores in colloform sphalerite, includes pyrite, arsenopyrite, sphalerite, cassiterite, canfieldite (can) and galena which are overgrown by pirquitasite-hocartite (pir-ho) and minor frankeite (frk). Note that pirquitasite contains abundant exsolution lamellae of stannite (stn) and locally contains inclusions of cassiterite and sphalerite. Galena is locally coated by fibrous frankeite (image "o")

6–8 wt%), but locally this trend can be reversed. Chemical data and interpretation of this texture is discussed in detail elsewhere (Slater et al. 2019).

Stage V

This stage consists of abundant massive sulfide accompanied by gangue minerals. The dominant minerals are pyrite, marcasite, quartz, cassiterite, clays, and siderite. Pyrite occurs as colloform interlayers with marcasite (Fig. 6d) and as individual grains or aggregates with a concentric zonation. Pyrite cores are inclusion free, whereas their growth zones often contain mineral inclusions (Slater et al. 2019). Quartz is euhedral and rarely has inclusions of cassiterite. Fibrous and feather-like orange sphalerite filling interstitial space is accompanied by acicular cassiterite. Siderite is predominantly seen in the upper levels of the ore zone peripheral to the central breccia vein and may have formed after earlier Fe-sulfides.

Stage VI

This stage is characterized by narrow veinlets (~ 1 mm; Figs. 5c, 6a and b) having abundant kesterite and pyrite and minor amounts of sphalerite, arsenopyrite, Ag-bearing tetrahedrite, miargyrite, pyrargyrite, and a Ag-Sb-Pb-bearing phase whose composition resembles Pb-bearing miargyrite (Slater et al. 2019). The Ag-bearing phases of tetrahedrite, miargyrite, and pyrargyrite are intergrown (Fig. 7j–l), whereas the Ag-Sb-Pb-bearing phase is found as rounded inclusions in miargyrite with diffuse boundaries. In this stage, kesterite is the dominant sulfosalt, whereas Ag-tetrahedrite is a minor phase. Tetrahedrite geothermometry for this stage yielded a temperature of 270 ± 10 °C (Slater et al. 2019).

Stage VII

This stage is characterized by an abundance of Sn-bearing sulfosalts and scarcity of Ag-Sb-bearing sulfosalts. The minerals of this stage, pyrite, sphalerite, arsenopyrite, galena, canfieldite, pirquitasite-hocartite, cassiterite, stannite and frankeite, line vugs, and pores in the earlier mineralization (Fig. 7m–o). The stage can be further broken into two substages with the first containing sphalerite, pyrite, cassiterite, arsenopyrite, galena, and canfieldite, whereas the second has minerals of the pirquitasite-hocartite series. Further details of these substages are discussed in Slater et al. (2019).

Stage VIII

This stage contains mineralization and alteration that may signify the waning of the hydrothermal system. Clays, mostly dickite, along with minor amounts of siderite, quartz, and hydrous phosphates, such as goyazite, line vugs, and occur in alteration selvages on the immediate wall rock. The siderite is anhedral and is inundated with inclusions of clay which suggests they are synchronous.

Fluid inclusions

Representative images of FIs and their host crystals are shown in Fig. 8. A summary of the microthermometric data is provided in Table 1 and in graphic form in Fig. 9 which consists bar graphs displaying the mean, range, and sample size for each of the 21 FIAs measured. The types of FIs, their classification, and thermometry results are discussed below.

Coarser crystals in colloform sphalerite from stage II contain two types of FIs—type 1 high-density two-phase liquid-vapor (L-V) and type 2 V-rich. Type 1 are regular to equant in shape, up to 30 μm in diameter and locally abundant (Fig. 8a). As FIs generally appear to decorate fracture planes and cut primary growth zones, they are considered to be secondary or pseudosecondary in origin (Fig. 8a, b). The FIAs have average $Tm_{(ice)}$ values between − 0.1 and − 2.9 °C, which equate to salinities between 0.2 and 4.8 wt% eq. NaCl. Based on observed eutectic temperatures (Te) between − 30 and − 24 °C, the chemistry of the FIs is best approximated by the H_2O-NaCl system (i.e., Te of − 21.1 °C), but with a small amount of undetermined divalent cations (e.g., Ca, Fe, Mg). The Th values range between 207 and 227 °C, and there is very little range within the FIAs (< 5–10°), except in one case (FIA 13). For the $Tm_{(ice)}$ data, there are low ranges for all FIAs. No positive correlation is noted between Th and $Tm_{(ice)}$, as average Th values do not vary significantly between different FIAs (Fig. 9).

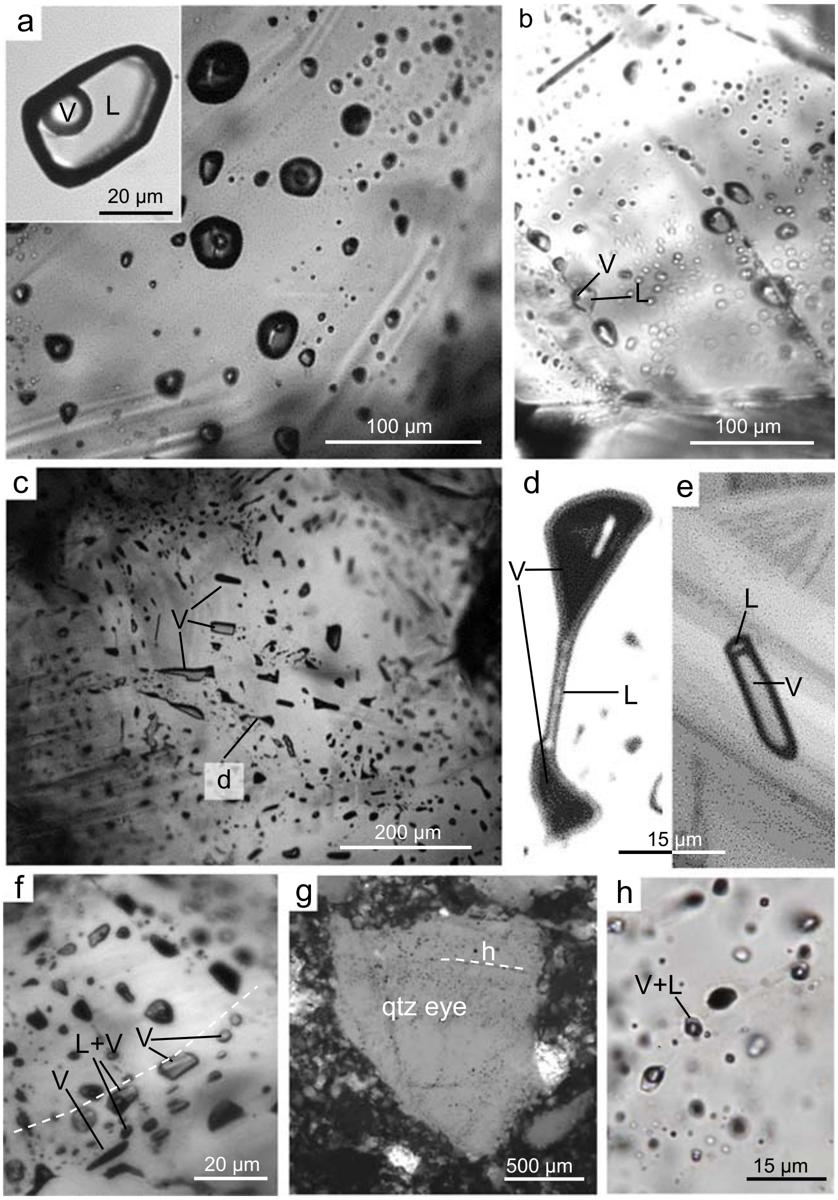

Fig. 8 Photomicrographs to illustrate the nature of FI in sphalerite (sph) and breccia-hosted quartz fragments. Note the FI in sphalerite were taken with infrared light. **a** Secondary or pseudosecondary (S/PS) L-rich FI in stage II sphalerite showing uniform size, shape and L-V ratios. Inset is an enlarged FI not in the focal plane. **b** Healed fracture decorated with S type L-rich FI in stage IV sphalerite. **c** Area of primary (P) vapor (V)-rich FI in growth zone of stage II sphalerite. Note location of image "d". **d**, **e** FI in area of image c with shapes suitable for microthermometry (see text for discussion). **f** Zone of P type FI in stage IV sphalerite with variable L:V ratios attributed to heterogeneous entrapment from a boiling fluid. **g** Anhedral quartz of unknown provenance in the Potosi Breccia North that is decorated with abundant S-type FI along annealed cracks (e.g., white dashed line). **h** S-type FI with roughly equal L:V ratios decorating a healed fracture. This is an enlarged part of image "g"

Type 2 V-rich FIs in stage II sphalerite are equant to irregular shaped, up to 30–40 µm, and generally occur along growth zones and thus are interpreted as primary (Fig. 8c–e). Importantly, these FIs do not coexist with L-rich types or FIs with variable L-V ratios; hence they likely represent entrapment of a low-density fluid. Although these are the most abundant FI type observed, most of these FIs do not have the prerequisite shape (i.e., horned or elongate; see discussion in Bodnar et al. (1985)) for Th determination. However, two such inclusions in the same sphalerite grain proved suitable (Fig. 8d, e) and thermometric measurements yielded Th values of 322 ± 0.2 °C and 340 ± 10 °C, with the associated errors in Th values reflecting repeated measurements and the difficulty in observing the exact moment of complete homogenization. As the first of these was more suitably shaped, it gave a more precise measurement (± 0.2 °C; Fig. 8d) compared with the second FI (±10 °C; Fig. 8e). Salinity data are not available for these FI.

Banded- to colloform-textured sphalerite of stage IV contains both FI types. Type 2 occur along growth zones and are therefore assigned a primary origin. In some cases, both FI types are present along growth zones (i.e., thus an FIA) with some having variable L-V ratios, but mostly V-rich (Fig. 8f), which suggests these FIs likely reflect entrapment of a boiling fluid with some heterogeneous entrapment possible. Type 1 FIs in several FIAs yielded $Tm_{(ice)}$ between −1.3° to −4.5 °C and Th values between 257 and 282 °C. Type 1 FIs also occur along annealed fractures which usually extend to grain boundaries and are thus assigned a secondary origin. These FIs have consistent L:V ratios and two FIAs yielded an average $Tm_{(ice)}$

Table 1 Fluid inclusion assemblage (FIA) microthermometric data summary for sphalerite

Stage	FIA	No. of inclusions measured	Type	V:L (Visual)	Long axis (µm)	TF (°C)	Te (°C)	Tm Ice (°C)	Th (°C)	Salinity (wt% NaCl equiv.)
Sample DDH-230C										
II	1	10	S/PS	0.15	22	−44.5		−2.8	209.1	4.68
II	2	3	S/PS	0.15	42			−2.8	212.3	4.65
II	3	6	S/PS	0.1	22	−50	−30	−2.7	213.7	4.54
II	4	4	S/PS	0.1	26		−24.3	−2.8	211.4	4.65
II	5	4	S/PS	0.13	28				203.3	
II	6	6	S/PS	0.15	15			−2.9	213.8	4.8
II	7	14	S/PS	0.1	18			−2.7	213.3	4.48
II	8	5	S/PS	0.1	32		−24.5	−1.4	208	2.37
II	9	1	S/PS	0.1	30		−25	−2.7	223.3	4.49
II	10	6	S/PS	0.1	29			−2.7	214.7	4.53
II	11	12	S/PS	0.15	21			−1.8	214.6	3.06
II	12	14	S/PS	0.1	16			−0.8	207.4	1.46
II	13	12	S/PS	0.15	37		−23.1	−0.5	214.2	0.88
II	14	5	S/PS	0.15	40			−1.1	207.7	1.91
II	15	1	S/PS	0.2	53			−0.1	227	0.18
II	N/A	1	P	0.95	50				322	
II	N/A	1	p	0.9	19				340	
Sample DDH-230I										
IV	16	4	S	0.2	15			−1.4	259.4	2.41
IV	17	3	S	0.2	15			−1.4	255.7	2.41
IV	18	3	P	0.2	7			−2.4	235.3	4.03
IV	19	1	P	0.2	20			−4.5	278.5	7.17
IV	20	2	P	0.2	35			−3	256.6	4.88
IV	21	5	P	0.2	20			−1.3	282.1	4.18

of −1.4 °C, or salinities of 2.4 wt% eq. NaCl, and similar Th values of 256 °C and 259 °C.

Sparse FIs in quartz are L-rich (L-V ratio 8 to 9:1) and similar to the type 1 secondary/pseudosecondary FIAs observed in sphalerite from both stages II and IV. In some exotic quartz fragments (i.e., broken quartz veins, quartz eyes) in a pebble-dyke breccia in Cortaderas and in the Potosi Breccia North, secondary FIAs are present (Fig. 8g, h). The FIs in these FIAs have higher V:L ratios (i.e., estimated visually at 0.4–0.6; Fig. 8h) and locally display heterogeneous entrapment. Although no thermometric data were obtained, based on their V:L ratios, it can be inferred that they were trapped at relatively high temperatures (e.g., from > 350 to 400 °C at low salinities; Roedder 1984; Becker et al. 2019).

Sulfur isotopes

Sulfur isotopic data for sphalerite and pyrite are reported for both mineral separates and in situ SIMS measurements. For sphalerite (Stage II) and pyrite (Stage I) separates, the results along with details of the samples are provided in Table 2. Sphalerite having both colloform and dendritic texture shows a small range in δ^{34}S values from 1.5 to 3.5‰ and average 2.4‰ (± 0.9, 1σ) with no correlation with textural variety. For pyrite, two samples of stage I have similar δ^{34}S values of 0.5 and −0.1‰, whereas the third sample, which is for diagenetic pyrite hosted in argillite country rock, has a much lower value at −28.8‰.

The results for the 16 in situ SIMS δ^{34}S measurements (ESM Table 2) were done as a continuous traverse through colloform-textured sphalerite (see ESM Fig. 2). The δ^{34}S values range from 0.9 to 5.2‰ and show no spatial variation in regard to texture or transparency of the material. The data average 3.6‰ (± 1.2, 1σ) which is similar to that for the sphalerite separates (2.4‰). The measured variation of about 4‰ contrasts with the spot-to-spot reproducibility of 0.4‰ based on analysis of the standard.

Discussion

The Cortaderas body is a mineralogically and texturally complex ore zone with a multistage paragenesis which

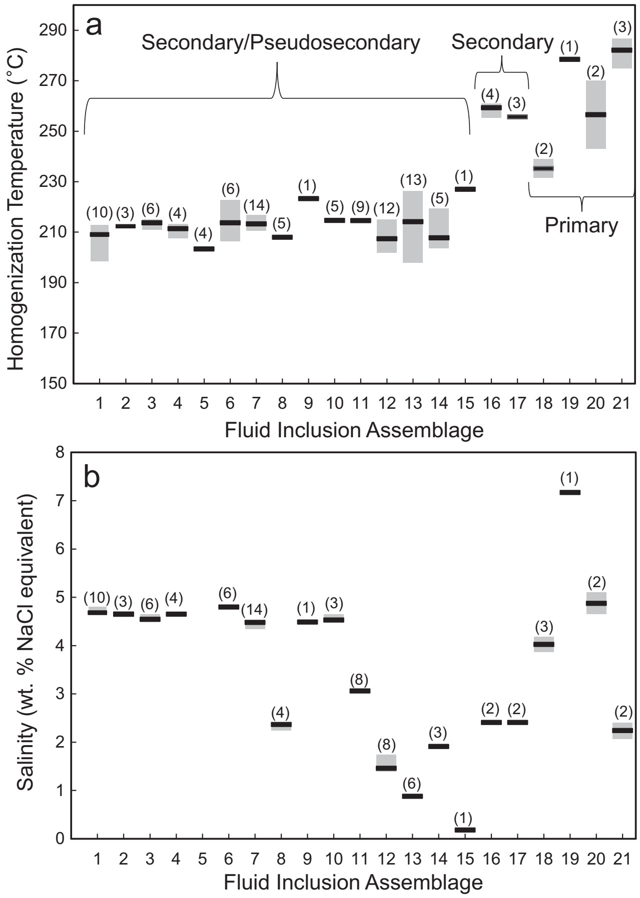

Fig. 9 The range and mean of thermometric data measured for FIs at Cortaderas. Note the number of FIs measured for each FAI is given in parenthesis. **a** Homogenization temperatures for each FIA. **b** Salinity (wt% eq. NaCl) for each FIA

reflects formation in an evolving dynamic hydrothermal system. Integration of our extensive data set for the different breccia types, including mineralogy, textures, FI and geochemistry, are used to generate a genetic deposit model. Furthermore, these data are compared with work on the Pirquitas deposit proper and the ATB in general to put the mineralization into a local and regional context.

Fluid inclusions

Inferred high-temperature type FIs (e.g., see Becker et al. 2019) in quartz from breccia samples in both Cortaderas and Pirquitas proper (i.e., Potosi Breccia North) are inferred to be sourced at depth from vein quartz and quartz megacrysts. These FIs are similar to unmixed, near-critical, or intermediate-type FIs seen in numerous high-level magmatic-hydrothermal systems, in particular porphyry systems (e.g., Bingham, Utah (Redmond et al. 2004), Dabaoshan, China (Mao et al. 2017)). Given the setting of the study area, these FI are considered to plausibly reflect the presence of putative felsic intrusion(s) at depth which underwent first and/or second boiling and inevitably fluid exsolution. That this relates to the hydrothermal systems which the breccias cut is conjectured without further evidence, but it is not inconsistent with the field setting and fact that the richly mineralized Pirquitas-Cortaderas deposits are clearly magmatic-hydrothermal in origin (this study; Desanois et al. 2017, 2018; Slater et al. 2019). Furthermore, these fluids may also equate to the FIs observed in stage I1 of the Pirquitas deposit noted by Desanois et al. (2018) which yielded Th values (i.e., not pressure corrected) of up to 370 °C. Early vein stages in Bolivian Sn-Ag deposits are also interpreted to have formed at temperatures up to 530 °C (Kelly and Turneaure 1970), as are the initial stages of the San Rafael deposit, SE Peru (Kontak and Clark 2002; Wagner et al. 2009). Thus, the noted FIs in the breccia-hosted quartz provide circumstantial evidence of a causative intrusion at depth.

Temperatures and related processes during stages II and IV at Cortaderas are well constrained with sphalerite-hosted FIs. The presence of nearly monophase populations of V-rich FIs without L-rich types in exceptionally well-preserved stage II sphalerite preclude an origin for such V-rich FIs due to post-entrapment modification or necking. Instead the V-rich FIs are attributed to a flashing system (i.e., trapped in the V-only field), in the same way Moncada et al. (2012, 2017) interpreted similar FIAs in the richly mineralized zones of the Guanajuato epithermal deposits, Mexico. Although Th data for V-rich FIs are limited, they provide maximum

Table 2 Sulfur isotopic data reported for mineral separates of sphalerite and pyrite

Sample	Material	δ^{34}S (‰, VCDT)	Origin	Texture
A-sph	Sph	1.7	Unclassified	Massive
DDH 214–323.86 m	Sph	2.8	Stage II	Colloform
DDH 214–323 m	Sph	2.6	Stage II	Colloform
DDH 214–239 m	Sph	1.5	Stage II	Massive
DDH 230–468 m	Sph	3.5	Stage II	Dendritic
DDH 230–440 m	Py	0.5	Stage I	Massive
DDH 230–471 m py	Py	− 0.1	Stage I	Massive
DDH 214–238 m py	Py	− 28.8	Diagenetic	Massive

conditions between 320 and 340 °C and constrain P_{fluid} (see below). Further corroborating evidence for fast boiling is found in the textures and presence of nano- to micro-inclusions of various sulfide phases in both sphalerite and zoned pyrite (see Slater et al. 2019) which, based on the recent detailed study of Roman et al. (2019) of pyrite in the active Cerro Pabellón geothermal system, Chile, is considered diagnostic of boiling in epithermal systems. In stage IV sphalerite, primary FIAs have Th values between 235 and 282 °C with a singular FIA recording heterogeneous entrapment at 282 °C. Thus, temperatures of 320 °C to 340 °C and 280 °C are assigned to stages II and IV, respectively, based on the present data set.

The temperature at which flashing occurred in stage II is elevated relative to temperatures of formation for stages III and VI determined using sulfosalt thermometry (Slater et al. 2019) and indicates the Ag-rich ores precipitated at lower temperatures than the Zn-rich ores. However, the ~280 °C temperature recorded for stage IV based on FIs is in line with that for stage VI determined by sulfosalt geothermometry (270 ± 10 °C: Slater et al. 2019) and thus validates the former and implies the Th data requires little if any pressure correction. The secondary/pseudosecondary FIAs of L + V observed in stage II sphalerite are compatible with fluids trapped between flashing events during quiescent intervals. Thus, whereas these FIs represent the majority of thermometric data collected, they are not interpreted to be most representative of the ore-forming conditions.

That flashing occurred at Cortaderas is important in regard to deposit genesis, as it implies cycling fluid pressure (e.g., Moncada et al. 2012, 2017). Such pressure fluctuations are related to transient dilation of the major structures that localized the mineralization, such as the fault breccia that preceded Cortaderas (Fig. 2a). These features provided conduits for overpressured fluids which formed the hydrothermal breccias that temporally and spatially overlap mineralization. This formational model is similar to the “fault valve” model of Sibson et al. (1988), which is widely applied to orogenic vein systems. The occurrence of large-scale brecciation, in addition to unusual disequilibrium-type textures (i.e., sphalerite dendrites), provides further support of fluid pressure cycling.

The primary FIAs in stage IV provide evidence of heterogeneous entrapment and thus constrain paleo-depth during mineralization. Using the Th of ~280 °C and salinity of 4.2 wt% eq. NaCl for this stage, trapping of the fluid on the L-V curve is constrained to ~65 bar (Fig. 10a) which, for a purely hydrostatic pressure gradient, equates to ~650 m below the paleo-water table. As this sample comes from ~400 m below the current base of the Cortaderas Valley, the top of the paleo-water table is estimated to have been ~250 m above the present valley bottom during stage IV mineralization. This depth is consistent with mineralization having formed after or during the late stages of the deposition of the Tiomayo Formation, the top of which is constrained to deposition at < 10 Ma (Coira et al. 2004).

The FI data, along with the elevated trace-metal signature of sphalerite and pyrite (e.g., As, Ag, Ge, In, Cu, Sn; Slater et al. 2019), are consistent with the ore fluid being of dominantly magmatic origin. Salinity for secondary/pseudosecondary FIAs in stages II sphalerite shows a mixing trend between a moderately saline fluid (4.5 to 5.0 wt% NaCl) and a dilute fluid (Fig. 10b) with both endmembers having Th values between ~200 and ~230 °C. These data are consistent with a moderately saline magmatic fluid being diluted with heated meteoric water or condensed vapor, with the former preferred as condensed vapor will have a greater salinity than these fluids record (< 1 wt% eq. NaCl; see Heinrich (2005) and Richards (2011)). These results are thus similar to the FIs measured by Desanois et al. (2018), particularly for the final, low-temperate stage of the Pirquitas deposit (Stage II in Malvicini 1978). The FIAs from stage IV sphalerite have up to 7 wt% NaCl, also consistent with a dominantly magmatic fluid.

In Bolivian Sn-Ag deposits (Kelly and Turneaure 1970; Sillitoe et al. 1975; Sugaki and Kitakaze 1988), as well as other global settings with granite-related Sn-W-base metal mineralization (e.g., San Rafael, Peru Sn-W (Kontak and Clark 2002; Wagner et al. 2009), Panasqueira, Portugal W(-Sn) (Kelly and Rye 1979), Mt. Pleasant, Canada (Samson 1990), Cornubian, SW England Sn-W (Hosking 1969; Jackson et al. 1989), and Korean W (So et al. 1991)), the temperatures and salinities of ore fluids have been shown to progressively decrease in the later stages of mineralization, which has been attributed to dilution by meteoric water. Similarly, Desanois et al. (2017, 2018) attribute the positive correlation between Th and fluid salinity in the Pirquitas deposit to dilution of an initial magmatic fluid by meteoric water. As these authors did not report phase separation (boiling), fluid mixing is likely the dominant ore forming process there. Similarly, there is some evidence for fluid mixing in Cortaderas which may account for some of its mineralization, as is common in epithermal settings. However, where the mineralization stages are characterized by abundant colloform and dendritic-textured sphalerite substantial and cyclical supersaturation related to flashing is the preferred mechanism for mineralization.

Sulfur isotopes

Discussing the first data for sphalerite, we note that the $\delta^{34}S$ values for both separates and SIMS analyses are similar with averages of 2.4‰ and 3.6‰, respectively. That the range for the in situ data of about 4‰ is greater than the spot-to-spot reproducibility (± 0.4‰) suggests a change in the $\delta^{34}S_{H2S}$ from which the sphalerite precipitated given the limited temperature dependent fractionation between

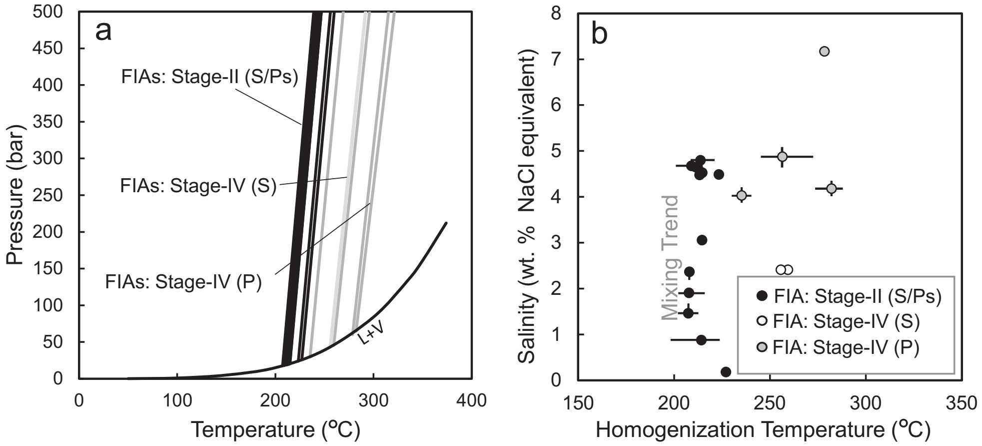

Fig. 10 **a** Isochores for each FIA from stage IV and II sphalerite. The boiling curve (i.e., L-V curve) for a 4.5 wt% NaCl fluid is shown as a curved black line. The isochores and L-V curve were calculated using HOKIELFINCS H2O-NaCl (Steele-MacInnis et al. 2012). **b** Plot of average salinity versus average homogenization temperature for each of the 21 FIAs measured. Note the distribution of the data for stage II sphalerite shows a mixing trend between a low-salinity fluid (~4.5 wt% eq. NaCl) and meteoric water which is not recorded for stage IV sphalerite data

sphalerite and H_2S at 250–300 °C (< 0.4‰; Ohmoto and Rye 1979). Two possible reasons for this variation are considered. The first is a change in fluid [SO_4:H_2S] which will affect the $\delta^{34}S$ value of precipitating sulfides (Ohmoto and Rye 1979). For the inferred temperature range of the mineralization of ca. 250–350 °C, excursions between $\delta^{34}S_{H2S}$ and $\delta^{34}S_{fluid}$ can be quite large (i.e., − 15 to − 20‰) as the pyrite-magnetite buffer is approached (Rye and Ohmoto 1974). Although the [SO_4:H_2S] of the fluid is not constrained, if this value increased in the ore fluid then there would be a commensurate drop in the value of $\delta^{34}S_{H2S}$ which would be inherited by the sphalerite. It also follows from this that the minimum $\delta^{34}S_{fluid}$ value would have to be the highest in situ measured $\delta^{34}S$ sphalerite value of 5.3‰. A second consideration relates to the anomalously low $\delta^{34}S$ value of − 28.8‰ for the wall rock hosted pyrite, which most likely relates to a biogenic sulfur reservoir. Thus, we cautiously suggest that some of this S may have been scavenged by the mineralizing fluids with mass balance suggesting a maximum of about 10% assuming a primary $\delta^{34}S_{H2S}$ signal of 5.3‰. Thus, at present, two scenarios are considered as possible explanations for the $\delta^{34}S$ sphalerite data.

Considering next the data for the hydrothermal pyrite, two points are noted: (1) the average value of 0.3‰ for the two analyses is lower than the minimum for sphalerite either by in situ (0.9‰) or by bulk (1.5‰) methods; and (2) isotopic discordance is suggested for pyrite and sphalerite given that $\Delta_{pyrite\text{-}sphalerite}$ at 300–350° = 1.5‰ (Ohmoto and Rye 1979). The latter can be explained however if, as suggested for the sphalerite, there has been a mixing of sulfur reservoirs. If this is considered, then it follows using the $\delta^{34}S$ value of 5.3‰ for sphalerite (see above) that pyrite in equilibrium with sphalerite would have had a $\delta^{34}S$ value of about 7‰. Thus, mass balance suggests mixing with 20% wall rock–derived sulfur to account for the pyrite $\delta^{34}S$ values.

Regardless of whether there was a change in the [SO_4:H_2S] of the ore fluid or mixing of S reservoirs, the $\delta^{34}S_{fluid}$ is considered to have a minimum value near 5‰ based on sphalerite (i.e., $\Delta_{sphalerte\text{-}H2S}$ at 300–350 °C ≈ 0‰). This value is consistent with those typical of crust-derived magmas and their derivative magmatic fluids (Ohmoto and Rye 1979; Ohmoto and Goldhaber 1997; Seal 2006) and, furthermore, comparable to $\delta^{34}S_{H2S}$ values for many Sn-W deposits globally (see Kontak (1990) for summary), and interestingly identical to the average for sulfides at San Rafael (Wagner et al. 2009). This value is in keeping with both a magmatic fluid source and its derivation from an evolved peraluminous magma having a significant crustal component, which is the preferred progenitor for the Sn-Ag ore systems of the ATB (Lehmann 1987; Lehmann et al. 1990).

Breccia bodies

Fault breccias observed adjacent to the central breccia vein are interpreted as reactivated Cretaceous faults (e.g., Cladouhos et al. 1994), hence similar to those in many other ore deposits (e.g., Sillitoe 1985, 2010). Here, fault breccia likely acted as a preexisting plane of weakness that focussed the dilation needed to accommodate the mineralized breccia. The fault breccias are not strongly mineralized except where replaced by pyrite in stage I, and thus they may have been locally impermeable. Idoyaga (1995) demonstrated that various veins at Pirquitas formed in fault jogs produced by strike-slip displacement. In Cortaderas, over-pressured fluids could have facilitated the reactivation of the preexisting fault in the Cortaderas Valley in a strike-slip manner creating dilation along bends in the structure.

Crackle, phreatic, and pebble-dyke breccias are interpreted to have genetic relationships in ore-forming systems. Crackle breccias, which are common features in hydrothermal systems, form due to changes in fluid pressure (Jébrak 1997). At Cortaderas, they likely formed due to depressurization and are related to dilation of the central structure. Similarly, phreatic- and pebble-dyke breccias generally form due to the sudden release of built-up fluid pressure triggered by events such as emplacement of intrusions or seismically induced faulting (Sillitoe 1985). At Cortaderas, emplacement of new intrusive stocks or rupturing of the outer carapace of a fractionating magma chamber could have released fluids and triggered the explosive emplacement of these fluidal breccias bodies at several stages in the paragenesis.

The presence of igneous clasts in phreatic and pebble-dyke breccias could have been caused by two processes: (1) descent of volcanic rock fragments from overlying Miocene ignimbrite deposits; or (2) ascent of fine-grained intrusive (subvolcanic) rock fragments from a buried Miocene intrusion. The latter process is favored for two reasons. Firstly, petrographic observations reveal that quartz in the clasts contains secondary FIAs with intermediate or near-critical L:V proportions, as discussed above. These fluids must have been trapped at temperatures and pressures too high to have been formed near the surface elevation. Secondly, pebble-dyke breccias in Cortaderas contain mineralization in rounded clasts that more closely resembles the mineralization at Pirquitas (e.g., colloform cassiterite). Thus, these observations strongly support the vertical ascent of material sourced at depth. Furthermore, the Potosi Breccia North has many characteristics of an intrusion breccia described by Sillitoe (1985), such as a rock flour matrix with a significant igneous component. It is likely that the Potosi Breccia North is rooted in an intrusion at depth, particularly where it is strongly clay and sericite altered. Sillitoe (1985) describes similar breccias at the Oruro deposit in Bolivia.

Origin of Colloform and dendritic textures

Colloform-textured sphalerite is often related to fluid mixing, such as in sediment-hosted Pb-Zn deposits (e.g., Barrie et al. 2009; Gagnevin et al. 2014; Boyce et al. 2015). Occurrences of colloform cassiterite, such as in the high-grade tin lode at San Rafael, SE Peru, resemble the colloform textured sphalerite at Cortaderas and are attributed to fluid mixing and saturation of cassiterite (e.g., Kontak and Clark 2002; Wagner et al. 2009). However, colloform-textured gangue phases in epithermal Au-Ag systems are commonly attributed to fast boiling or flashing (e.g., Simmons et al. 2005; Moncada et al. 2012, 2017; Taksavasu et al. 2018 and references therein). In Cortaderas, flashing is the preferred mechanism for colloform sphalerite formation, but as there is also some evidence for fluid mixing, it is possible that this process contributed to sphalerite supersaturation. We further explore the origin of colloform-textured sphalerite below and its association with dendritic textures.

Data on the origin of colloform pyrite and marcasite is limited, as FI studies were not possible for these minerals. Franchini et al. (2015) argue that colloform pyrite and marcasite in the Agua Rica deposit, Catamarca, Argentina, formed due to undercooling that was facilitated by boiling. The colloform pyrite and marcasite in Cortaderas could have also been formed by boiling of a fluid depleted in Zn, but it could also have formed by fluid mixing.

Dendritic-textured (also elongate and spindly) minerals are described in a wide variety of settings which include hydrothermal fluids and silicate melts. Although sulfides with such textures are not commonly documented, examples are found in sediment-hosted Pb-Zn deposits and sea-floor vent sites (Paradis et al. 1988). Similar textures are prevalent in epithermal settings as bladed calcite and adularia where they are attributed to boiling (e.g., Simmons et al. 2005; Marinova et al. 2014; Moncada et al. 2012, 2017 and references therein). In addition, fine- to coarse-grained dendritic gold, electrum, and naumannite (Ag_2Se) are also found in these settings (e.g., Sherlock and Lehrman 1995; Saunders 1994, 2012). Dendritic textures are also common in silicate systems such as pegmatites, where several mineral phases develop this habit (e.g., K-feldspar, muscovite, spodumene, tourmaline; London and Kontak (2012) and references therein), and ultramafic rocks, where spinifex textures are widespread (e.g., olivine and clinopyroxene: Faure et al. 2006; Welsch et al. 2012). The observation that both skeletal phases and colloform or banded textures form simultaneously in pegmatite settings, as suggested from both natural settings (e.g., London 2008; Kontak et al. 2002) and experimental studies (London 2008, 2009), provides further relevance to the ore textures at Cortaderas. The latter is particularly relevant to the similar intimate coupling of colloform and dendritic textures, in this case for sphalerite, at Cortaderas (Fig. 6c). The aforementioned examples of dendritic-like textures reflect different settings, bulk chemistries, and even processes (i.e., fluid mixing in the sea floor settings, slow or fast boiling in hydrothermal systems, undercooling in silicate melts, aggregation of nanoparticles for gold), but in all cases, rapid precipitation and mineral growth occur in response to changing physiochemical conditions. Thus, by analogy with other settings, we suggest that the most likely reason for the formation of dendritic sphalerite and its association with colloform textures is fast boiling or flashing which typifies epithermal settings rather than undercooling in silicate systems. There is a lack of FI data for the dendritic sphalerite; however, we presented above FI data supporting a flashing model for the colloform sphalerite. Due to its association with colloform textures, dendritic sphalerite is interpreted to have formed in a similar manner. Lastly, we note that Simmons and Browne (1997) provide FI evidence for sphalerite deposition in a boiling geothermal well in Broadlands, New Zealand, showing that boiling is an effective mechanism for precipitating sphalerite.

Ore minerals

Except for a minor amount of Ag-bearing galena, sulfosalts are the only minerals that host wt% levels of Ag at Cortaderas. Silver-bearing sulfosalts occur in four of the eight paragenetic stages (II, III, VI, and VII). Stage II mineralization hosts Ag as blebby inclusions of proustite in galena. This stage likely only accounts for minor Ag as it is diluted by abundant co-genetic sphalerite and pyrite. Stage III mineralization, consisting of Ag-bearing tetrahedrite, pyrargyrite, miargyrite, and minor unidentified phases, accounts for the majority of Ag when present. Stage VI mineralization, which is similar to stage III, is volumetrically minor and thus does not account for significant Ag. Lastly, stage VII mineralization, the principal Sn-sulfosalt-bearing stage, appears to account for a dispersal halo of low-grade Ag mineralization around Cortaderas and is not a dominant Ag stage.

The mineral assemblage present in stage III mineralization is typical for deposits in the southern portion of the ATB, such as Cerro Rico de Potosi, which also has abundant Ag-Sb-bearing sulfosalts (Turneaure 1960a, b). This high-grade Ag stage closely resembles that of stage II at Pirquitas which Desanois et al. (2017, 2018) attributed to fluid mixing. This is further supported by our observations that it formed immediately after a brecciation event at lower temperatures than the main sphalerite stage and also contained fine-grained cassiterite (Fig. 7h).

The mineral assemblage that composes stage VII mineralization differs from those of previous stages in that sulfides and sulfosalts, not cassiterite, host the majority of Sn. It is also unique in that it did not post-date a brecciation event. Its mineralogy resembles that of other zones at the Pirquitas mine, such as the stage I2 mineralization in the Oploca Veins, which are characterized by abundant minerals of the pirquitasite-hocartite series, as well as frankeite (Malvicini 1978; Desanois et al. 2017, 2018). This stage is interpreted to have formed at relatively high temperatures during a period of quiescence, possibly when the hydrothermal system was sealed, recharged, and dominated by reduced magmatic fluids under sufficient confining pressure as to not boil.

Slater et al. (2019) proposed that many of the current sulfosalt assemblages in several paragenetic stages could have been the product of unmixing during retrograde cooling; thus, they represent secondary rather than primary assemblages. They noted that the elements which were abundant in the main ore stages (Ag, Cu, Sb, and Bi) are readily incorporated into galena at high temperatures and speculated that these elements may have been released from a reservoir of galena at depth. Evidence for such a reservoir below Cortaderas includes the occurrence of rounded clasts with Ag-bearing galena in pebble dyke breccias interpreted to have been transported from depth. For Pirquitas, Desanois et al. (2018) inferred the presence of a similar deeper-situated Ag-rich mineralization at depth based on FI evidence.

Gangue minerals and alteration

Gangue phases may be a minor part of mineralization at Cortaderas, but they provide constraints on conditions attending mineralization. For example, the dickite that generally forms below 250 °C (Hedenquist et al. 2000), provides a rough upper thermal limit to stages V and VIII. In Bolivian Sn-Ag deposits, siderite is a common alteration product of Fe-sulfides, such as pyrrhotite, and is constrained from FI studies to typically form between 200 and 260 °C (Kelly and Turneaure 1970). Thus, the presence of both siderite and dickite in stages V and VIII suggests formation temperatures of 200 °C to 250 °C. Hydrous phosphates in the late stages of Bolivian Sn-Ag mineralization are attributed to both hypogene and supergene origins (Kelly and Turneaure 1970). Goyazite and REE-bearing hydrous phosphates at Cortaderas are attributed a hypogene origin based on their intergrowth with minerals such as cassiterite and may signify neutralization of the hydrothermal fluids due to the ingress of meteoric water.

Metal zonation

Metal zonation is common in Sn deposits (Turneaure 1971; Taylor 1979), as it is in other ore settings (e.g., VMS and porphyry). Typically, the higher temperature Sn-Cu ore zones transition to lower temperature Zn-Pb-Ag ore zones with the later either overprinting the former or being more distal (Turneaure 1971; Taylor 1979). The metal distribution at Pirquitas and Cortaderas suggests a thermal gradient with inferred higher temperature Sn-rich ore focussed in the San Miguel zone and Zn-rich ore found distally at Cortaderas. Contrary to this simplistic model, however, are the FI and sulfosalt thermometric data which show no appreciable differences between temperature or salinity at Cortaderas and Pirquitas. Further complicating this is the telescoped nature of the ore zones and varied mineralogy at both Cortaderas and Pirquitas which suggests varied temperatures.

At the scale of Cortaderas, it appears however that metals do not show a zoned distribution. Silver, Zn, Sn, and Pb are concentrated below the 4200 m level, which could be the result of vertically restricted boiling and flashing. Structures such as the Cortaderas fault and the closure of a N-S trending antiform appear to have focused mineralization and may also have acted as conduits for mineralizing fluids, but also as aquitards in restricting some of the mineralization. As a general trend, Ag, Zn, and Sn all increase in concentration with depth suggesting that mineralization continues below the currently tested depths. The Ag-Zn-rich mineralization in Cortaderas may also give way to Pirquitas-style Ag-Sn-rich mineralization at greater depths; an inference supported by the presence of Ag-Sn-rich rounded clasts in pebble dyke breccias interpreted to have been transported from below.

Ore-zone classification

The mineral assemblages in sulfide-rich hydrothermal ore deposits reflect the prevailing sulfidation state of the fluid, itself a function of various intensive parameters (e.g., sulfur fugacity, temperature; Barton Jr. and Skinner 1967; Einaudi et al. 2003). Cortaderas represents a hydrothermal system in which mixing of dominantly magmatic fluids and external meteoric fluids occurred such that the physicochemical conditions, including sulfidation state, fluctuated, as noted in other epithermal settings (e.g., Rottier et al. 2018; Wang et al. 2019). For the purposes of classifying the ore zone, the temperature of stage II, as determined by microthermometry, is used in conjunction with its mineralogy (Fig. 7; also see Slater et al. 2019) to assess the sulfidation state of the system (Fig. 11). The exclusive appearance of Ag in sulfosalts indicates sulfur fugacity and temperature combined to inhibit the formation of native Ag. Furthermore, the presence of tetrahedrite and absence of enargite and famatinite constrain sulfidation state to below this reaction boundary. The intermittent formation of arsenopyrite, which forms in low-sulfidation conditions, suggests oscillating conditions between intermediate- and low-sulfidation states and might reflect a wall rock influence, which is not inconsistent with the δ^{34}S data above. Furthermore, such oscillations in physiochemical conditions and thus sulfidation state are not uncommon in Andean polymetallic epithermal systems (e.g., Baumgartner et al. 2008; Benedezú and Fontboté 2009; Rottier et al. 2018).

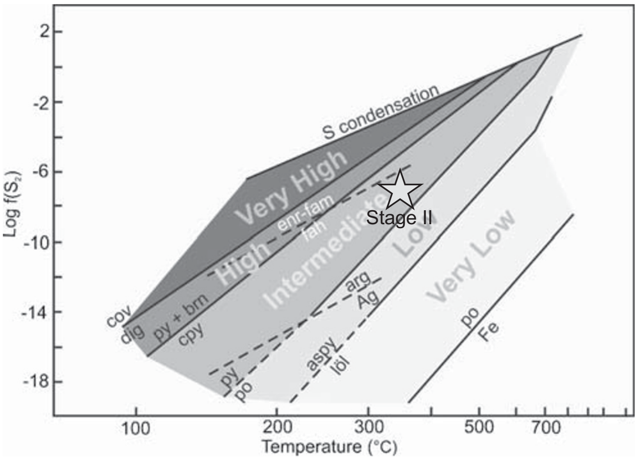

Fig. 11 Epithermal classification diagram based on sulfidation state. Here temperature is plotted against sulfur fugacity and the stability fields of some relevant minerals are shown. (modified from Einaudi et al. 2003). The mineralogy and temperature estimated for stage II, the main Zn stage and denoted by the star, is used to constrain the sulfidation state. py pyrite, brn bournite, cpy chalcopyrite, cov covellite, dig digenite, brn bornite, löl löllingite, arg argentite, fah fahlore, enr-fam enargite-famatinite

Genetic model

Collectively, the data presented and discussed above supports a model whereby the Cortaderas deposit resulted from episodic release of a magmatic-sourced ore fluid generated from a postulated underlying felsic magma. Transient depressurization, facilitated by reactivation of earlier faults and its epizonal setting, resulted in flashing and boiling of the fluid. This model is schematically illustrated in Fig. 12 for the first two stages of the paragenesis and, in general, is similar to that suggested for Pirquitas by Desanois et al. (2017, 2018) and other polymetallic Sn-bearing deposits in the Andes (e.g., Kelly and Turneaure 1970). However, an important departure from Desanois et al. (2017, 2018) relates to the lack of evidence for fluid unmixing in the Pirquitas system; hence, they suggested fluid mixing was the key ore forming process. That Cortaderas and Pirquitas are separated by some 500 m and have slightly different vein orientations may account for the noted differences in ore elements, ore textures, deposit geometry (i.e., Pirquitas veins versus Cortaderas breccias), and fluid characteristics.

Shown schematically in the model is the presence of a Cretaceous-age fault below what is now the Cortaderas Valley. This fault was likely reactivated in a strike-slip manner possibly due to the combined effects of the inferred intrusion underlying the Pirquitas area, including associated fluid pressure, and far-field stresses such as plate convergence or destabilization during uplift of the Puna. Given the lack of evidence for a high-salinity fluid, as in other Sn-W systems of the ATB (Kelly and Turneaure 1970) or porphyry-type deposits in general (e.g., Richards 2011), it is apparent that fluid ascent followed the deep contraction path of Hedenquist et al. (1998; see Richards (2011) for discussion) above the critical curve in the H_2O-NaCl system. Upon ascent to the shallow ore environment (i.e., < 700 m), the ore fluids flashed or boiled, as dictated by the confining pressure, which favored development of disequilibrium-type textures (i.e., colloform and dendritic). Dilation along this structure also facilitated ingress of meteoric fluids which were first passively heated and then intermittently mixed with magmatic fluids. The formation of sulfide-rich mineralization as the result of flashing, boiling, and later fluid mixing sealed the system allowing temperatures and pressures to rise. During prolonged states of quiescence in a sealed system where thermal advection dominated and temperature gradients were highest, earlier Zn- and Ag-Sb-rich mineralization which formed in the open system was overprinted by Ag-Sn-sulfosalts (e.g.,

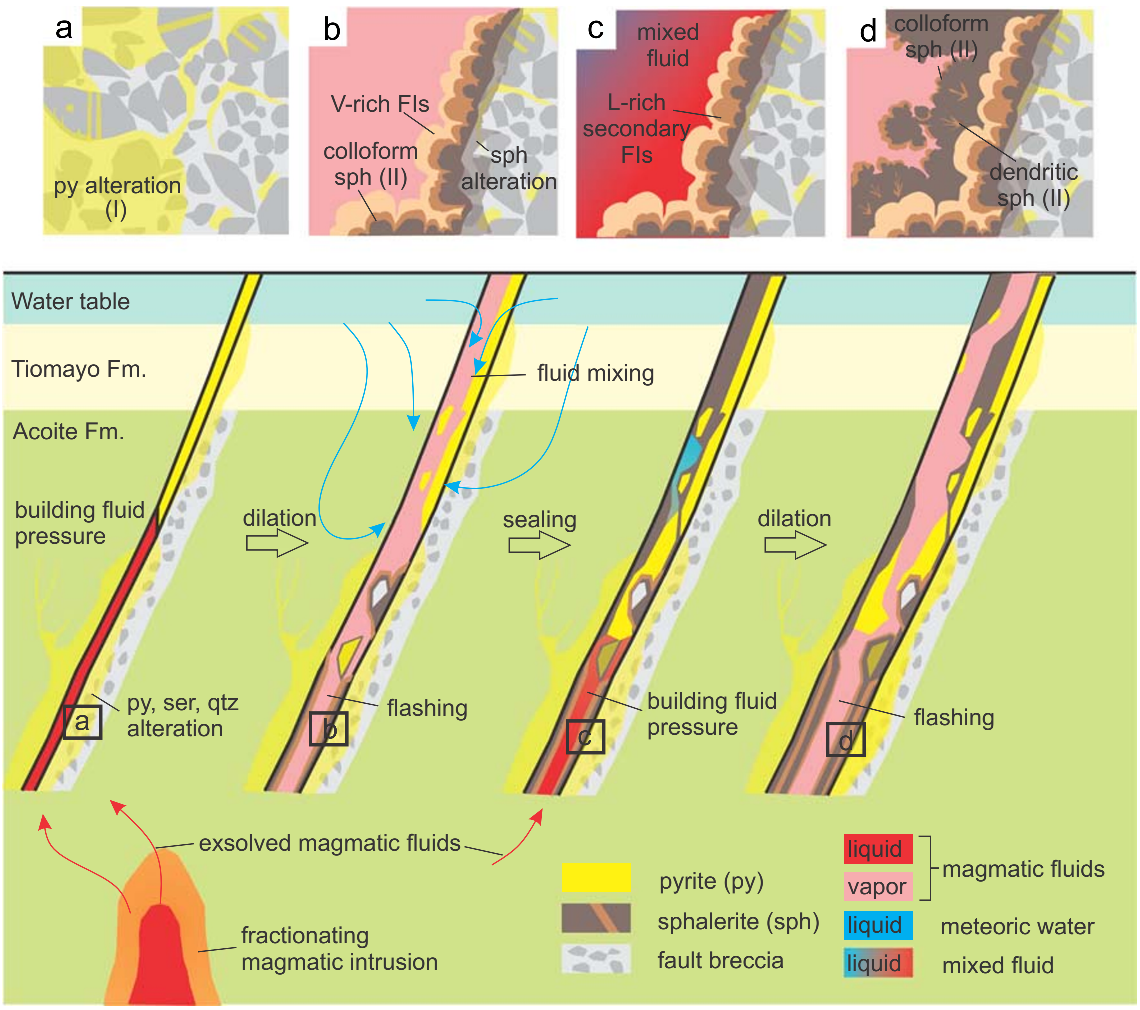

Fig. 12 Schematic genetic model illustrating the early stages of mineralization in the Cortaderas Breccia body. The boxes labeled "a" through "d" are magnified views of inset boxes in the larger diagram. **a** A preexisting fault breccia zone is reactivated due to the build-up of fluid pressure related to an inferred, evolving magma body at depth. The periodic release of acidic fluids penetrates the wall rocks to form a pyrite, sericite, and quartz alteration. Early mineralization creates a seal allowing for further buildup of fluid pressure. **b** The dilation of the system and related breccia formation is commensurate with the magmatic fluids undergoing sudden depressurization and flashing to steam. In a vertically restricted zone, the flashing results in the rapid precipitation of colloform- and dendritic-textured sphalerite which host V-rich FI. This structure also serves as a conduit for descending meteoric water which mixes with magmatic fluids to form mineralization and sealing of the structure. **c** Fluid pressure again rises in the now sealed structure. Secondary/pseudosecondary FI with moderate density is trapped in the sphalerite preserving evidence of fluid mixing. **d** The system again dilates and brecciates causing the dominantly magmatic fluid to flash to steam with further formation, albeit in a restricted zone, of dendritic-and colloform-textured sphalerite

stage VII). Subsequent increase in fluid pressure eventually exceeded the tensile strength of the sulfide seal and resulted in more dilation, brecciation, and mineralization. Subsolidus unmixing of the mixed sulfide-sulfosalt-oxide assemblage resulted in the complex mineral assemblage noted above, as was discussed in detail by Slater et al. (2019). The proposed model involving cycling of magmatic fluid ingress, dilation, and sealing of the main structure, and likely periodic ingress of meteoric water, is similar to the "fault valve" model of Sibson et al. (1988), as applied to orogenic gold systems, or also the recent shake-up model of Richards (2018).

Conclusions

The structurally controlled Ag-Zn-Pb-Sn-mineralized Cortaderas Breccia body peripheral to the Pirquitas deposit area was the product of an intermediate sulfidation epithermal system fed by an unexposed but inferred underlying evolved crust-derived felsic magma. Mineralization developed over eight paragenetic stages that included initial rock preparation (I), several ore events (II-VII) with inter-mineral brecciation, and a waning period (VIII); the key characteristics of the mineralization are summarized in Table 3. The system episodically depressurized following dilation and brecciation that resulted in "flashing" of ascending magmatically sourced fluids.

Table 3 Summary of characteristic of the Cortaderas Breccia zone

Ore zone characteristics		Evidence
Hydrothermal fluids	Magmatic (4.5 to 7.0 wt% NaCl equivalent)	Fluid inclusions
	Meteoric (No salinity)	Fluid inclusions
Temperature	Rock preparation and pyritization: > 350 °C	Fluid inclusions petrography (estimated)
	Principal Zn stage: > 320 °C	Fluid inclusion microthermometry (V-rich FI)
	Principal Ag-stages: 245 ± 15 °C and 270 ± 10 °C	Fahlore thermometry (Slater 2016, Slater et al. 2019).
	Waning stages: ~ 200 °C to ~ 250 °C	Mineralogy (dickite and marcasite)
		Fluid inclusions (secondary)
Source of sulfur	Magmatic fluids	SIMS
Ore-forming processes	Flashing, boiling, fluid mixing	Fluid inclusions, textures
Post-ore erosion	~ 250 m (assuming hydrostatic gradient)	Fluid inclusions
Mineralization	Pyrite, marcasite, sphalerite, arsenopyrite, cassiterite, quartz, clays (dickite), galena, siderite, sulfosalts	Petrography, SEM-EDS, EMP, powdered XRD
Alteration	Silica, clay (dickite ± kaolinite), sericite, chlorite, goyazite, REE-bearing hydrous phosphates	Petrography, SEM-EDS, powdered XRD
Textures	Massive, colloform, dendritic, cockade	Petrography
Breccias	Fault, crackle, phreatic, pebble-dykes	Petrography
Intrusion	Unidentified. Potosi Breccia North may be connected to a buried intrusion at depth and has a large igneous component	Porphyritic clasts
Age	< 15.7 ± 0.6 Ma	Crosscutting relationship with Tiomayo Fm

The evidence used to make the interpretations are indicated

The latter resulted in rapid precipitation of sulfide minerals and formation of colloform and dendritic textures; it may also have contributed to Ag mineralization; however, fluid mixing was also likely important for forming Ag-rich ores. Stage VII mineralization, characterized by Ag-Sn-bearing sulfosalts, formed during a quiescent period when the system was sealed and temperature gradients were higher reflecting the telescoped nature of the ore system. The abundant clay alteration is hypogene in origin and occurred during the late stages of mineralization. The magmatic-sourced fluids, heat, metals, and S for the Cortaderas Breccia system were likely derived from the same evolving magma chamber whose exsolved fluids fed the breccias and veins at the main Pirquitas deposit. Contrasting ore-forming processes at Cortaderas (flashing and boiling) and Pirquitas (fluid mixing) may account for why the former is Zn-rich and contains lesser Ag and Sn than the latter.

Acknowledgments We thank SSR Mining, (previously Silver Standard Resources Inc.) and its management, including Carl Edwards and Ronald Burk (formerly of Silver Standard), for providing access to the site, providing relevant information used in this paper, and funding during the course of the field work. We are also grateful to the exploration team at Mina Pirquitas that included Nicholas Larcher, Juan Terrazas, Javier Ceballos, Angus Innes, Carlos Juarez and Jorge Peralta for their invaluable assistance and discussions on the geology of the mine and surrounding area. Additional funding for this research was procured from an NSERC Discovery Grant to Dr. Kontak, as well as a Society of Economic Geologists Canada Foundation Research Grant to E. Slater. Sulfur isotope data was collected by R. Sharp at the University of Manitoba. The electron microprobe was operated with the assistance of Dr. K. Ross whereas the SEM was managed by Dr. William Zhe, both in the Microanalytical Centre (MAC) of Laurentian University. The Fluid Inclusion Lab at Laurentian University was funded by an NSERC Tools and Instruments (RTI) Grant to Dr. Kontak. Journal reviewers, L. Fontboté and G. Sosa, and editorial handling by B. Lehmann are sincerely thanked for constructive input and suggestions which resulted in clarification and significant improvements to the manuscript.

References

Bahlburg H (1990) The Ordovician basin in the Puna of NW Argentina and N Chile: geodynamic evolution from back-arc to foreland basin. Geotekt Forsch 75:1–107

Barrie CD, Boyce AJ, Boyle AP, Williams PJ, Blake K, Wilkinson JJ, Lowther M, McDermott P, Prior DJ (2009) On the growth of colloform textures: a case study of sphalerite from the Galmoy ore body, Ireland. J Geol Soc 166:563–582

Barton PB Jr, Skinner BJ (1967) Sulfide mineral stabilities. In: Barnes HL (ed) Geochemistry of hydrothermal ore deposits. Holt, Rinehart and Winston, New York, pp 236–333

Baumgartner R, Fontboté L, Vennemann T (2008) Mineral zoning and geochemistry of epithermal polymetallic Zn-Pb-Ag-Cu-Bi mineralization at Cerro de Pasco, Peru. Econ Geol 103:492–537

Becker SP, Bodnar RJ, Reynolds TJ (2019) Temporal and spatial variations in characteristics of fluid inclusions in epizonal magmatic-hydrothermal systems: applications in exploration for porphyry copper deposits. J Geochem Explor 204:240–255

Benedezú R, Fontboté L (2009) Cordilleran epithermal Cu-Zn-Pb-(Au-Ag) mineralization in the Colquijirca District, Central Peru: deposit-scale mineralogical patterns. Econ Geol 104:905–944

Board WS, Kennedy RB, Yeomans TJ (2011) NI 43-101 technical report on the Pirquitas mine, Jujuy, Argentina 1–220

Bodnar RJ, Reynolds TJ, Kuehn CA (1985) Fluid inclusion systematics in epithermal systems. In geology and geochemistry of epithermal systems, Berger, BR, Bethke PM (eds), Society of Economic Geologists, Reviews in Economic Geology, 2, p. 73–98

Boyce A, Barrie CD, Samson IM, Williams-Jones AE (2015) Aspects of the geochemistry of zinc – a journey to Sphalerite. In: Archibald SM, Piercy SJ (eds) Current perspectives on Zn deposits. Irish Association for Economic Geology, Geological Survey of Ireland, Dublin, pp 17–35

Caffe PJ, Trumbull RB, Coira BL, Romer RL (2002) Petrogenesis of early Neogene magmatism I the northern Puna; implications for magma genesis and crustal processes in the central Andean plateau. J Pet 43:907–942

Caffe PJ, Soler MM, Coira BL, Onoe AT, Cordani UG (2008) The Granada ignimbrite: a compound pyroclastic unit and its relationship with Upper Miocene caldera volcanism in the northern Puna. J S Am Earth Sci 25:464–484

Cladouhos TT, Allmendinger RW, Coira B, Farrar E (1994) Late Cenezoic deformation in the Central Andes: fault kinematics from the northern Puna, northwestern Argentina and southwestern Bolivia. J S Am Earth Sci 7:209–228

Clark AH, Farrar E, Caelles JC, Haynes SJ, Lortie RB, McBride SL, Quirt GS, Robertson RCR, Zentilli M (1976) Petrogenesis of early Neogene magmatism I the northern Puna: a progress report. Geol Assoc Can Spec Pap 14:23–58

Clark AH, Kontak DJ, Farrar E (1990) The San Judas Tadeo W(-Mo, Au) deposit: Permian lithophile mineralization in southeastern Peru. Econ Geol 85:1651–1668

Coira B (1979) Descripción geológica de la hoja 3c Abra Pampa, provincia de Jujuy. Boletín del Servicio Geológico Nacional 170: 1–90

Coira B, Caffe P, Ramírez A, Chayle W, Díaz A, Rosas S, Pérez A, Pérez B, Orozco O, Martínez M (2004) Programa nacional de cartas geológicas de la República Argentina. Hojas Geológica 2366-I/ 2166-III: Institutue de Geológía y Recursos Minerales 1–125

Cunningham CG, Zartman RE, McKee EH, Rye RO, Naeser CW, Sanjinés OV, Erickson GE, Tavera VF (1996) The age and thermal history of Cerro Rico de Potosi, Bolivia. Mineral Deposita 3:374–385

Desanois L, Lüders V, Trumbull, R (2017) Fluid inclusion studies in ore minerals from the polymetallic epithermal Sn-Ag Pirquitas deposit, Jujuy Province, NW Argentina. 14th SGA Biennial Meeting – Mineral Resources to Discover 1:343–346

Desanois L, Lüders V, Niedermann S, Trumbull RB (2018) Formation of epithermal Sn-Ag-(Zn) vein-type mineralization at the Pirquitas deposit, NW Argentina: Fluid inclusion and noble gas isotopic constraints. Chemical Geology 1:78-91

Einaudi MT, Hedenquist JW, Inan EE (2003) Sulfidation state of fluids in active and extinct hydrothermal systems: transitions from porphyry to epithermal environments. Society of Economic Geologists Special Publication 10:285–313

Farrar E, Yamamura BK, Clark AH, Tapie JA (1990) 40Ar/39Ar ages of magmantism and tungsten-polymentallic mineralization, Palca 11, Choquene District, southeastern Peru. Econ Geol 85:1669–1676

Faure F, Arndt N, Libourel G (2006) Formation of spinifex texture in Komatiites: an experimental study. J Petrol 47:1591–1610

Franchini M, McFarlane C, Maydagán L, Reich M, Lentz DR, Meinert L, Bouhier V (2015) Trace metals in pyrite and marcasite from the Agua Rica porphyry-high sulfidation epithermal deposit, Catamarca, Argentina: textural features and metal zoning at the porphyry to epithermal transition. Ore Geol Rev 66:366–387

Gagnevin D, Menuge JF, Kronz A, Barrie C, Boyce AJ (2014) Minor elements in layered sphalerite as a record of fluid origin, mixing, and crystallization in the Navan Zn-Pb ore deposit, Ireland. Econ Geol 109:1513–1528

Gamarra-Urrunaga JE, Castroviejo R, Bernhardt HJ (2013) Preliminary mineralogy and ore petrology of the intermediate-sulfidation Pallancata deposit, Ayacucho, Peru. Can Mineral 51:67–91

Goldstein RH, Reynolds TJ (1994) Systematics of fluid inclusions in diagenetic minerals. Society for Sedimentary Geology Short Course 31:1–199

Harrington HJ (1957) Ordovician formations of Argentina. In: Harrington HJ, Leanza AF (eds) Ordovician trilobites of Argentina, Kansas: University of Kansas Paleontological Contributions Special Publication 1. University of Kansas Press, pp 1–59

Hedenquist JW, Arribas RA Jr., Reynolds TJ (1998) Evolution of an intrusion-centered hydrothermal system: Far Southeast-Lepanto porphyry and epithermal Cu-Au deposits, Philippines. Econ Geol 93:373–404

Hedenquist JW, Arribas AJ, Gonzales-Urien E (2000) Exploration for epithermal gold deposits. Rev Econ Geol 13:245–277

Heinrich CA (1990) The chemistry of hydrothermal tin(−tungsten) ore deposition. Econ Geol 85:457–481

Heinrich CA (2005) The physical and chemical evolution of low-salinity magmatic fluids at the porphyry to epithermal transition: a thermodynamic study. Mineral Deposita 39:864–889

Hosking KFG (1969) The nature of primary tin ores of the south-west of England: a conference on tin, Bangkok, International Tin Council 1: 245–266

Idoyaga MG (1995) Caracterización tectónica y metalogénica de los depósitos estanníferos argentinos. Dissertation, Universidad de Buenos Aires

Jackson NJ, Willis-Richard J, Manning DC, Sams MS (1989) Evolution of the Cornubian ore field, Southwest England: Part II. Mineral deposits and ore-forming processes. Econ Geol 84:1101–1133

Jébrak M (1997) Hydrothermal breccias in vein-type ore deposits: a review of mechanisms, morphology, and size distribution. Ore Geol Rev 12:111–134

Kay SM, Mpodozis C (2001) Central Andean ore deposits linked to evolving shallow subduction systems and thickening crust. GSA Today 11:4–9

Kelly WC, Rye RO (1979) Geologic, fluid inclusion, and stable isotope studies of the tin-tungsten deposits of Panasqueira, Portugal. Econ Geol 74:1721–1822

Kelly WC, Turneaure FS (1970) Mineralogy, paragenesis and geothermometry of the tin and tungsten deposits of the eastern Andes, Bolivia. Econ Geol 65:609–680

Kittl E (1972) Yacimientos minerales y su formación: Revista Minera. Geología y Mineralogía 31:1–241

Kontak DJ (1990) A sulfur isotope study of main-stage tin and base metal mineralization at East Kemptville tin deposit, Yarmouth County, Nova Scotia, Canada: evidence for magmatic origin of metals and sulfur: Economic Geology 85:399–407

Kontak DJ, Clark AH (2002) Genesis of the giant, bonanza San Rafael lode tin deposit, Peru: origin and significance of pervasive alteration. Econ Geol 97:1741–1777

Kontak DJ, Dostal J, Kyser TK, Archibald DA (2002) A petrological, geochemical, isotopic and fluid inclusion study of 370 Ma pegmatite-aplite sheets, Peggy's Cove, Nova Scotia, Canada. Can Mineral 40:1249–1286

Lehmann B (1987) Tin granites, geochemical heritage, magmatic differentiation. Geol Rundsch 76:177–185

Lehmann B, Petersen U, Santavañez L, Winkelmann (1988) Distribución geoquímica de estaño y boro en la secuencia Paleozoic de la Cordillera Real de Bolivia. Bol Soc Geo Peru 77:19–27

Lehmann B, Ishihara S, Michel H, Miller J, Rapela CW, Sanchez A, Tistl M, Winkelmann L (1990) The Bolivian Tin Province and regional tin distribution in the Central Andes: a reassessment. Econ Geol 85: 1044–1058

Linnen RL, Pichavant M, Holtz F, Burgess S (1995) The effect of on the solubility, diffusion, and speciation of tin in haplogranitic melt at 850°C and 2 kbar. Geochim Cosmochim Acta 59(8):1579–1588

London D (2008) Pegmatites, vol 10. Canadian Mineralogist Special Publication, p 368

London D (2009) The origin of primary textures in granitic pegmatites. Can Mineral 47:697–724

London D, Kontak DJ (2012) Granitic pegmatites: scientific wonders and economic bonanzas. Elements 8(4):257–262

Malvicini L (1978) Las vetas de estaño y plata de Mina Pirquitas (Pircas) provencia de Jujuy, República Argentina. Revista de la Asociación Argentina de Mineralogía, Petrología y Sedimentología 9:1–25

Mao W, Rusk B, Yang F, Zhang M (2017) Physical and chemical evolution of the Dabaoshan porphyry Mo deposit, South China: insights from fluid inclusions, cathodoluminescence, and trace elements in quartz. Econ Geol 112:889–918

Marinova I, Ganev V, Titorenkova R (2014) Colloidal origin of colloform-banded textures in the Paleogene low-sulfidation Khan Krum gold deposit, SE Bulgaria. Mineral Deposita 49:49–74

Marrett RA, Allmendinger RW, Alonso RN, Drake RE (1994) Late Cenozoic tectonic evolution of the Puna Plateau and adjacent foreland, northwestern Argentine Andes. J S Am Earth Sci 7:179–207

Mlynarczyk MS, Williams-Jones AE (2005) The role of collisional tectonics in the metallogeny of the Central Andean Tin Belt. Earth Planet Sci Lett 240:656–667

Moncada D, Mutchler S, Nieto A, Reynold TJ, Rimstidt JD, Bodnar RJ (2012) Mineral textures and fluid inclusion petrography of the epithermal Ag-Au deposits at Guanajuato, Mexico: application to exploration. J Geochem Explor 114:20–35

Moncada D, Baker D, Bodnar RJ (2017) Mineralogical, petrographic and fluid inclusion evidence for the link between boiling and epithermal Ag-Au mineralization in the La Luz area, Guanajuato Mining District, México. Ore Geol Rev 89:143–170

Ohmoto H, Goldhaber MB (1997) Sulfur and carbon isotopes. In: Barnes HL (ed) Geochemistry of Hydrothermal Ore Deposits, 3rd edn. Wiley, New York, pp 517–611

Ohmoto H, Rye RO (1979) Isotopes of sulfur and carbon. In: Barnes HL (ed) Geochemestry of Hydrothermal deposits. Wiley, pp 509–567

Paar WH, Brodtkorb MK, Sureda RJ, Topa D (2001) Mineralogía, y quimismo de sulfuros y sulfosales de estaño y plomo en las vetas de Mina Pirquitas, Jujuy, Argentina (22°41'S66°28'W). Rev Geol Chile 28:259–268

Paradis S, Jonasson IR, Le Cheminant GM, Watkinson DH (1988) Two zinc-rich chimneys from the plume site, southern Juan de Fuca ridge. Can Mineral 26:637–654

Petersen U (1970) Metallogenic provinces in South America. Geol Rundsch 59:834–897

Redmond PB, Einaudi MT, Inan EE, Landtwing MR, Heinrich CA (2004) Copper deposition by fluid cooling in intrusion-centered systems: new insights from the Bingham porphyry ore deposit, Utah. Geology 32:217–220

Richards J (2011) Magmatic to hydrothermal metal fluxes in convergent and collided margins. Ore Geol Rev 40:1–26

Richards J (2018) A shake-up in the porphyry world. Econ Geol 113: 1225–1233

Roedder E (1984) 1984. Fluid inclusions. In Reviews in mineralogy, Vol 12, Ribbe, PH (ed), Mineralogical Society of America, Washington, D.C., 644 p.

Roman N, Reich M, Leisen M, Morata D, Barra F, Deditius AP (2019) Geochemical and micro-textural fingerprints of boiling in pyrite. Geochim Cosmochim Acta 246:60–85

Rosas LV, Avila JC (2013) Desarrollo minero de Pirquitas, provincia de Jujuy. Serie Correlación Geológica 29:51–62

Rottier B, Kouzmanov K, Casanova V, Wälle M, Fontboté L (2018) Cyclic dilution of magmatic metal-rich hypersaline fluids by magmatic low-salinity fluid: a major process generating the giant epithermal polymetallic deposit of Cerro de Pasco, Peru. Econ Geol 113:825–856

Rye RO, Ohmoto H (1974) Sulfur and carbon isotopes and ore genesis: A review. Econ Geol 69:826–842

Samson I (1990) Fluid evolution and mineralization in a subvolcanic granite stock: the Mount Pleasant W-Mo-Sn deposits, New Brunswick, Canada. Econ Geol 85:145–163

Saunders JA (1994) Silica and gold textures in bonanza ores of the sleeper deposit, Humboldt County, Nevada: evidence for colloids and implications for epithermal ore-forming process. Econ Geol 89:628–638

Saunders JA (2012) Textural evidence of episodic introduction of metallic nanoparticles into bonanza epithermal ores. Minerals 2:228–243

Schneider HJ, Lehmann B (1977) Contribution to a new genetic concept on the Bolivian tin province. In: Klemm DD, Schneider HJ (eds) Time- and strata-bound ore deposits, 1st edn. Springer-Verlag, Berlin, pp 153–168

Schuiling RD (1967) Tin belts on the continents around the Atlantic Ocean. Econ Geol 62:540–550

Seal RR (2006) Sulfur isotope geochemistry of sulfide minerals. Rev Mineral Geochem 61:633–677

Sherlock RL, Lehrman NJ (1995) Occurrences of dendritic gold at the McLaughlin Mine hot-spring gold deposit. Mineral Deposita 30: 323–327

Sibson RH, Robert F, Poulsen KH (1988) High-angle reverse faults, fluid-pressure cycling, and mesothermal gold-quartz deposits. Geology 16:551–555

Sillitoe RH (1972) Relation of metal provinces in western America to subduction of oceanic lithosphere: Geological Society of America 83:813–818

Sillitoe RH (1985) Ore-related Breccias in volcanoplutonic arcs. Econ Geol 80:1467–1514

Sillitoe RH (2003) Iron oxide-copper-gold deposits: an Andean view. Mineral Deposita 38:787–812

Sillitoe RH (2010) Porphyry copper systems. Econ Geol 105:3–41

Sillitoe RH, Perello J (2005) Andean copper province; tectonomagmatic settings, deposit types, metallogeny, exploration and discovery. Economic Geology. 100th anniversary volume 845–890

Sillitoe RH, Halls C, Grant JN (1975) Porphyry tin deposits in Bolivia. Econ Geol 70:913–927

Simmons SF, Browne PRL (1997) Saline fluid inclusions in sphalerite from the Broadlands-Ohaaki geothermal system: a coincidental trapping of fluids being boiled toward dryness. Econ Geol 92:485–489

Simmons SF, White NC, John DA (2005) Geological characteristics of epithermal precious and base metal deposits. Economic Geology, 100th Aniversary volume 485–522

Slater ET (2016) The origin of Ag-Zn-Sn mineralization in the Cortaderas deposit, Pirquitas mine, NW Argentina. M.Sc. thesis, Laurentian University, Sudbury, Canada, 1–112

Slater ET, McDonald AM, Kontak DJ (2019) Resolving primary and retrograde sulfide and sulfosalt textures in the epithermal Ag-Zn-Pb-Sn-rich Cortaderas zone, Pirquitas mine, Argentina. Can Mineral 57:117–143

So CS, Shelton KL, Chi SJ, Yun ST (1991) Geochemical studies of the Gyeongchang W-Mo mine, Republic of Korea: progressive meteoric water inundation of a magmatic hydrothermal system. Econ Geol 86:750–767

Soler MM, Caffe PJ, Coira BL, Onoe AT, Kay MS (2007) Geology of the Vilma caldera: a new interpretation of a large-scale explosive event in the central Andean plateau during the Upper Miocene. J Volcanol Geotherm Res 164:27–53

Steele-MacInnis M, Lecumberri-Sanchez P, Bodnar RJ (2012) HOKIEFLINCS_H2O-NACL: a Microsoft Excel spreadsheet for interpreting microthermometric data from fluid inclusions based on the PVTX properties of H_2O-NaCl. Comput Therm Sci 49: 334–337

Sugaki A, Kitakaze A (1988) Tin-bearing minerals from Bolivian polymetallic deposits and their mineralization stages. Mining Geology 38:419–435

Taksavasu T, Monecke T, Reynolds TJ (2018) Textural characteristics of noncrystalline silica in sinters and quartz veins: implications for the formation of bonanza veins in low-sulfidation epithermal deposits. Minerals 8:331–249

Taylor RG (1979) Geology of tin deposits, vol 11. Dev Econ Geol, p 543

Turneaure FS (1960a) A comparative study of major ore deposits of Central Bolivia. Part I. Econ Geol 55:217–254

Turneaure FS (1960b) A comparative study of major ore deposits of Central Bolivia. Part II. Econ Geol 55:574–606

Turneaure FS (1971) The Bolivian tin-silver province. Econ Geol 55: 215–225

Turner JC (1982) Descripción geológica de la hoja 3b, Mina Pirquitas, Jujuy Servicio Geológico Nacional Secretaría de Industria y Minería Boletín 187:1–56

Turner JC, Mendez V (1979) Puna: Segundo simposio de geologia regional argentina, Córdoba, Academia Nacional de Ciencias 13–56

Wagner T, Mlynarczyk MS, Williams-Jones AE, Boyce AJ (2009) Stable isotope constraints on ore formation at the San Rafael tin-copper deposit, Southeast Peru. Econ Geol 104:223–248

Wang L, Ke-Zhang Q, Guo-Xue S, Guang-Ming L (2019) A review of intermediate sulfidation epithermal deposits and subclassification. Ore Geol Rev 107:434–456

Welsch B, Faure F, Famin V, Baronnet A, Bachèlery P (2012) Dendritic crystallization: a single process for all the textures of olivine in basalts? J Petrol:1–36

Publisher's note Springer Nature remains neutral with regard to jurisdictional claims in published maps and institutional affiliations.